

# Chemical abundances in LMC stellar populations

## I. The Inner disk sample <sup>\*</sup>

Luciana Pompéia<sup>1,2</sup>, Vanessa Hill<sup>3</sup>, Monique Spite<sup>3</sup>, Andrew Cole<sup>4,5</sup>, Francesca Primas<sup>6</sup>, Martino Romaniello<sup>6</sup>, Luca Pasquini<sup>6</sup> Maria-Rosa Cioni<sup>7</sup> and Tammy Smecker Hane<sup>8</sup>

<sup>1</sup> IP&D, Universidade do Vale do Paraíba, Av. Shishima Hifumi, 2911, São, José dos Campos, 12244-000 SP, Brazil

<sup>2</sup> Instituto Astronômico e Geofísico (USP), Rua do Matão 1226, Cidade Universitária, 05508-900 São Paulo, Brazil  
e-mail: pompeia@univap.br

<sup>3</sup> Observatoire de Paris-Meudon, GEPI and CNRS UMR 8111, 92125 Meudon Cedex, France  
e-mail: Vanessa.Hill@obspm.fr e-mail: Monique.Spite@obspm.fr

<sup>4</sup> School of Mathematics and Physics, University of Tasmania, Private Bag 37, Hobart, TAS 7001, Australia

<sup>5</sup> Kapteyn Astronomical Institute, University of Groningen, Postbus 800, NL-9700 AV Groningen, Netherlands  
e-mail: cole@astro.rug.nl

<sup>6</sup> European Southern Observatory, Karl Schwarzschild Str. 2, 85748 Garching b. München, Germany  
e-mail: fprimas@eso.org e-mail: mromanie@eso.org e-mail: lpasquin@eso.org

<sup>7</sup> Edinburg SUPA, School of Physics, University of Edinburgh, IfA, Blackford Hill, Edinburgh EH9 3HJ, UK  
e-mail: mrc@roe.ac.uk

<sup>8</sup> Department of Physics and Astronomy, 4129 Frederick Reines Hall, University of California, Irvine, CA 92697-4575  
e-mail: smecker@carina.ps.uci.edu

Received/Accepted

**Abstract.** *Aims.* We have used FLAMES (the Fibre Large Array Multi Element Spectrograph) at the VLT-UT2 telescope to obtain spectra of a large sample of red giant stars from the Inner Disk of the LMC,  $\sim 2$  kpc from the center of the galaxy. We investigate the chemical abundances of key elements for the under-

standing of the star formation and evolution of the LMC disk: heavy and light [ $s$ -process/Fe] and  $[\alpha/\text{Fe}]$  give constraints on the time-scales of formation of the stellar population. Cu, Na, Sc and the iron-peak elements are also studied aiming to better understand the build up of the elements of this population and the origin of these elements. We aim to provide a more complete picture of the LMC's evolution by compiling a large sample of field star abundances.

*Methods.* LTE abundances are derived using line spectrum synthesis or equivalent width analysis. We have used OSMARCS model atmospheres and an updated line list.

*Results.* We have found that the alpha-elements Ca, Si, and Ti show lower  $[X/\text{Fe}]$  ratios than Galactic stars at the same  $[\text{Fe}/\text{H}]$ , with most  $[\text{Ca}/\text{Fe}]$  being subsolar.  $[\text{O}/\text{Fe}]$  and  $[\text{Mg}/\text{Fe}]$  ratios are slightly deficient, with Mg showing some overlap with the Galactic distribution. Sc and Na follow the underabundant behavior of Ca, with subsolar distributions. For the light  $s$ -process elements Y and Zr, we have found underabundant values compared to their Galactic counterparts.  $[\text{La}/\text{Fe}]$  ratios are slightly overabundant relative to the galactic pattern showing low scatter, while the  $[\text{Ba}/\text{Fe}]$  are enhanced, with a slight increasing trend for metallicities  $[\text{Fe}/\text{H}] > -1$  dex. The  $[\text{heavy-}s/\text{light-}s]$  ratios are high, showing a slow increasing trend with metallicity. We were surprised to find an offset for three of the iron-peak elements. We have found an offset for the  $[\text{iron-peak}/\text{Fe}]$  ratios of Ni, Cr and Co, with an underabundant pattern and subsolar values, while Vanadium ratios track the solar value. Copper shows very low abundances in our sample for all metallicities, compatible with those of the Galaxy only for the most metal-poor stars. The overall chemical distributions of this LMC sample indicates a slower star formation history relative to that of the solar neighborhood, with a higher contribution from Type Ia supernovae relative to Type II supernovae.

**Key words.** Stars: abundances, Galaxies: Magellanic Clouds, Galaxies: abundances, Galaxies: evolution

## 1. Introduction

During the last decade, due to the operation of the new class of large telescopes, we have witnessed for the first time the analysis of elemental abundances of large samples of individual stars in external galaxies. Thanks to new optical technologies, objects fainter than supergiant stars, planetary nebulae or HII regions are now possible targets suitable for extragalactic research, allowing the study of older objects and the exploration of earlier phases of galaxy evolution. The abundance patterns of diverse elements in numerous stars in a galaxy give information on different domains such as the kinematic and chemical

---

*Send offprint requests to:* L. Pompeia, e-mail: [pompeia@univap.br](mailto:pompeia@univap.br)

\* Based on observations collected at the VLT UT2 telescope (072.B-0608 and 066.B-0331 programs), Chile.

evolution, nucleosynthesis channels, the star formation history (SFH) and the initial mass function (IMF) of its stellar population(s).

One of the most interesting extragalactic objects in the study of stellar populations is the Large Magellanic Cloud (LMC), our nearest companion after the Sagittarius dwarf galaxy (that is the process of merging with the Milky Way). The LMC is an irregular galaxy located within 50 kpc from the Sun, with a kinematically-defined disk, a bar and a thick disk or flattened halo (e.g. Westerland 1997). The almost face-on position of its disk, with a tilt relative to the plane of the sky of  $\sim 30^\circ$ , gives us the precious opportunity to study stars from its different components.

The star formation (SF) and cluster formation histories of this galaxy have been studied for more than three decades (e.g. Butcher 1977, van den Bergh 1979, Olszewski et al. 1996 and references therein, Cioni et al. 2006 and references therein) although a final picture is far from complete (the current status of the research deals with the detailed SF and cluster formation within the different components and regions of this galaxy, e.g. Geha et al. 1998, Smecker-Hane 2002, Subramaniam 2004, Javiel et al. 2005, Cole et al. 2005). The clusters of the LMC show an ancient population with ages  $> 11.5$  Gyr, followed by an hiatus when just one single cluster seems to have formed (ESO 121-SC03) (e.g. van den Bergh 1998 and references therein). Some 2-4 Gyr ago, a new formation event was triggered and some other clusters have been built (e.g. Da Costa 1991). The SF in the disk field shows a different evolution, with nearly constant rate over most of the history of the LMC (Geha et al. 1998). The SFR appears to have been enhanced some 1-4 Gyr ago, with the timing and amplitude of the ‘burst’ seeming to vary between locations (Holtzman et al. 1999; Olsen et al. 1999). The SFH of the bar field appears to more closely track the cluster formation history, with a strong burst  $\approx 3-6$  Gyr ago (Smecker-Hane et al. 2002; Cole et al. 2005). The lack of a field star age gap means that field star properties can be used to trace the history of the LMC during the 3-11 Gyr cluster age gap (Da Costa 1999; van den Bergh 1999).

The elemental distributions of the LMC stars are still poorly known, due to the paucity of data, but the present picture is in fast change due to new observational programs (e.g. Evans et al. 2005, Dufton et al. 2006, Johnson et al. 2006). We briefly summarize here the results on elemental abundances in the LMC (for a detailed discussion see Hill 2004). The abundance analysis of B stars and HII regions (Garnett 1999, Korn et al. 2002, Rolleston et al. 2002) show a deficient abundance of O, Mg and Si relative to their solar neighborhood counterparts<sup>1</sup>, with mean  $\log (X/H) - \log (X/H)_\odot \sim -0.2$  dex for oxygen,  $-0.2$  dex for magnesium, and  $-0.4$  dex for silicon abundances (this last value is only for the B stars, HII regions show a much lower value of  $\sim -0.8$  dex), but compatible to galactic supergiant values. Russell & Dopita (1992), Hill et al. (1995) and Luck

<sup>1</sup> taking as the solar value  $\log (O/H) \sim 8.83$  (Grevesse & Sauval 2000)

et al. (1998) studied samples of supergiants in the field of the LMC and Hill & Spite (1999) derived abundances for supergiants in clusters. They found a similar behavior for the  $\alpha$ -elements when compared to the galactic disk values, while for the heavy elements (those with  $Z \geq 56$ ), the abundance ratios are enhanced by a factor of  $\sim 2$ . Huter et al. (2007) derived C, Mg, O, Si and N abundances for three globular clusters from the LMC, and found an average value 0.3 dex lower than that of the Galactic Clusters for all the analysed elements, except for N. Red giant branch stars from the field (Smith et al. 2000, hereafter SM02) and from globular clusters (Hill et al. 2000, 2003, hereafter H00 and H03, and Johnson et al. 2006, hereafter JIS06) have also been studied. A general behavior of low  $[\alpha/\text{Fe}]$  ratios compared to the stars of the galactic disk with similar metallicities is detected (with the exception of Si and Mg in JIS06), while for the heavy-elements, the same overabundant pattern found for the LMC supergiants has been derived. JIS06 inferred the  $[\text{Y}/\text{Fe}]$  ratios and found abundances compatible to the solar value. Na abundances are different in field and clusters stars. While SM02 found low  $[\text{Na}/\text{Fe}]$  ratios and  $[\text{Sc}/\text{Fe}]$  ratios close to zero, JIS06 found that  $[\text{Sc}/\text{Fe}]$  and  $[\text{Na}/\text{Fe}]$  ratios are similar to their galactic counterparts. JIS06 have derived the [iron-peak/Fe] abundances and found that Ni, V and Cu abundances fall below their corresponding galactic values.

An observational project aiming at making the full analysis of the elemental abundances of significant samples ( $\sim 70$ -100) of stars from different locations in the LMC has been developed, taking advantage of the FLAMES multiplex facility at the VLT. We have obtained spectra from stars in three different regions of the LMC: the Inner Disk (characterised by a galactocentric radius of  $R_C=2\text{kpc}$ ); the Outer Disk (with  $R_C=4\text{kpc}$ ); and a field near the optical center of the Bar. Stars have been selected based on kinematics and metallicity data derived from the near-infrared calcium triplet (CaT and CaT metallicities), trying to sample as evenly as possible the whole metallicity range of this galaxy. In the present paper we focus on a sample of Red Giant Branch (RGB) stars on the Inner Disk region, previously studied by Smecker-Hane et al. (2002), who derived the ages, metallicities (CaT) and kinematics of this sample. They have identified two kinematical groups in the Inner Disk field, one with velocity dispersion of  $13\pm 4$  km/s, characterizing a thin disk, and one with velocity dispersion of  $34\pm 6$  km/s, probably pertaining to the flattened halo. The metallicities of these two groups are different: the low-dispersion velocity group has metallicities ranging  $-0.6 \leq [\text{Fe}/\text{H}] \leq -0.3$  dex, while the high-dispersion velocity component has  $-2 \leq [\text{Fe}/\text{H}] \leq -0.4$ . The ages derived for this Inner Disk population has shown that stars have continuously formed during the last  $\sim 1$  to 15 Gyr, with a possible enhancement in the star formation rate (SFR) some 3 Gyr ago.

As the prototype galaxy of the Magellanic irregular class, to learn the evolutionary history of the LMC is clearly a vital step towards the global understanding of galaxies near the dwarf-giant boundary. Additionally, because the Magellanic Clouds have evolved

in such close proximity to the Milky Way, their histories have been intimately tied to that of our own galaxy. The ongoing impact of the LMC on the structure and kinematics of the Milky Way is manifest in the warp of the Galactic disk and possibly in the presence of the central bar (e.g., Weinberg 1999), while Bekki & Chiba (2005) have used N-body simulations to show that the LMC could have made a significant contribution to the build up of the Milky Way halo as a result of tidal stripping.

According to models of galaxy formation within a hierarchical CDM scenario (D’Onghia & Lake 2004; Moore et al. 1999), the history of the Milky Way depends strongly on its interactions with its environment. It now seems that the abundance patterns in dwarf spheroidal stars are dissimilar to those in Milky Way halo stars (e.g., Shetrone et al. 2001; Tolstoy et al. 2003; Geisler et al. 2005), ruling them out as analogues to the accreting fragments that built up the halo. Study of the LMC takes on added significance in this light, because of the hypothesis by Robertson et al. (2005) that the accretion of LMC-like fragments circumvents this difficulty with the hierarchical accretion scenario. Deeper knowledge of the abundances in the oldest LMC stars therefore has direct bearing on the evolution of our own Galaxy.

In the present paper, we focus on a sample of RGB stars in the Inner Disk field, previously studied by Smecker-Hane et al. (2002, hereafter SMH02), who derived the SFH of the region from Hubble Space Telescope color-magnitude diagrams; they find stars in this field to have formed continuously over the whole life of the LMC, with a slight enhancement in the star formation rate (SFR)  $\approx 3$  Gyr ago. Smecker-Hane et al. (2007) obtained CaT spectra for a large number of red giants to measure their kinematics and overall heavy element abundances, finding the most metal-rich stars to belong to a kinematically cold population and the metal-poor stars to be more kinematically hot, possibly belonging to a flattened halo or very thick disk population. We focus our work on the Inner Disk region, presenting abundance results for iron-peak, heavy and light  $s$ -process elements, and  $\alpha$  elements for a total of 59 stars. With this detailed information in hand, we aim to shed light on the following questions: (i) what are the chemical abundance patterns of the Inner Disk of the LMC?; (ii) what do these elemental distributions tell us about the formation and evolution of the LMC?; (iii) are they similar to any component of the Milky Way?; (iv) or to the populations of other Local Group galaxies?; (v) based on the elemental distributions, is a merging scenario with LMC debris a likely solution for the Galactic Halo formation?

The paper is organized as follows: in Sect. 2 the observations and the reduction procedure are described; in Sect. 3 the calculation of stellar parameters is presented; Sect. 4 describes the abundance determination procedures; Sect. 5 reports the results for the abundance ratios, comparing to Milky Way samples; in Sect. 6 we compare our results to those for the dSph galaxies; we discuss the results in Sect. 7; and finally in Sect. 8 a summary of the work is given.

## 2. Sample selection, observations and reductions

### 2.1. Sample selection

To best measure the elemental abundances of the LMC disk and their evolution along time, we selected a field located  $1.7^\circ$  southwest of the LMC Bar, in the Bar's minor axis direction to ensure a negligible contribution of its stellar populations. An HST color-magnitude diagram study of this field (SMH02) found it to have experienced a rather smooth and continuous history of star formation over the past 13 Gyr, with a possibly increased star-formation rate over the last 2 Gyr. This stands in contrast to the history of the Bar itself, in which significant star-formation episodes are seen to have commenced 4–6 Gyr ago (SMH02; see also Holtzman et al. 1999 and references therein). This field has also more recently been the target of a low-resolution spectroscopy campaign (Cole et al. 2000; SMH), using the CaT to derive its metallicity distribution and break the age-metallicity degeneracy inherent to color magnitude diagram CMD analyses.

We have used these infrared CaT metallicities from SMH to select a sample of red giant branch members of the LMC (based on their radial velocities) distributed uniformly (i.e., with the same number of stars in each metallicity bin) over the whole metallicity range of the LMC disk. In this way, we have been able to sample the lower metallicity bins of the LMC very efficiently. The most metal-poor stars convey essential information on the evolution of the elements of this galaxy, but they are rare, hence their number would have been significantly lower if we had selected our sample by picking stars randomly across the RGB. The final sample consists of 67 stars with CaT metallicities ranging from  $-1.76$  to  $-0.02$  dex (including 13 stars with metallicities below  $-1.0$  dex), drawn from the 115-star sample of SMH. In Fig. 1 we show the sample stars overplotted on the color-magnitude diagram of the LMC inner disk region (CTIO photometry from SMH). The sample mean magnitude is  $V=17.25$  mag, bright enough to allow reasonable S/N high-resolution spectra to be acquired.

### 2.2. Observations and reductions

The observations were made at the VLT Kueyen (UT2) telescope at Paranal during the Science Verification of FLAMES/GIRAFFE (Pasquini et al. 2000) in January, February and March, 2003, complemented by one night of the Paris Observatory Guaranteed Time Observations in January, 2004. In its MEDUSA mode, GIRAFFE is a multiobject spectrograph with 131 fibers of which 67 were used for the present project. The remaining fibers were allocated to targets of other Science Verification projects in the LMC. The detector is a  $2048 \times 4096$  EEV CCD with  $15\mu\text{m}$  pixels. We used the high resolution grating of GIRAFFE in three different setups: (i) H14  $\lambda 638.3 - \lambda 662.6$  nm with  $R=28800$ ; (ii) H13  $\lambda 612.0 - \lambda 640.6$  nm with  $R=22500$ , and (iii) H11  $\lambda 559.7 - \lambda 584.0$  nm with  $R=18529$ .

Exposure times are 6 hours for H14 and H13 setups and 7h30 for H11. The setups were chosen in order to cover the maximum number of key elements such as Fe I and Fe II for spectroscopic calculations of stellar parameters, and  $\alpha$ , iron-peak and *s*-process elements, for the abundance analysis. The average signal to noise ratio of the spectra is  $S/N \sim 80$  per resolution element.

The data reduction was carried out using the BLDRS (GIRAFFE Base-Line Data Reduction Software <http://girbldrs.sourceforge.net/>) and consists of bias subtraction, localization and extraction of the spectra, wavelength calibration and rebinning. We have also used the MIDAS packages for sky subtraction and co-addition of individual exposures.

### 3. Determination of stellar parameters

#### 3.1. Photometric stellar parameters

A first guess of the stellar parameters was made using photometric data of CTIO (V,I from SHM) and 2MASS (J,H,K). Bolometric magnitudes and effective temperatures were derived from calibrations of Bessell, Castelli & Plez (1998, hereafter BCP). The observed CTIO and 2MASS colors were transformed into the corresponding photometric systems using Fernie (1983, V–I Cousins to Johnson) and Carpenter (2001, K, V–K & J–K 2MASS). Photometric data are given in Table 1, while Table 2 gives the derived effective temperatures ( $T_{\text{phot}}$ ) and surface gravities ( $\log g_{\text{phot}}$ ):  $T_{\text{phot}}$  is derived using the BCP calibration of the dereddened V–I and V–K colors, and the surface gravity is computed using the following relation:

$$\log g_{\text{phot}} = 4.44 + \log(M) + 4 \times \log(T_{\text{phot}}/5790.) + 0.4 \times (M_{\text{bol}} - 4.75),$$

where  $M_{\text{bol}}$  is computed from the dereddened K magnitude of the star, the bolometric correction  $BC_K$  taken from BCP, and the mass of the stars ( $M$ ) are assumed to be  $2M_{\odot}$ . A distance modulus based on Hipparcos data and the period-luminosity relations from LMC Cepheids of  $18.44 \pm 0.05$  mag is assumed (Westerlund 1997, Madore & Freedman 1998). Uncertainties of this value stems from the specific subsets of the Cepheids chosen for the comparison (Madore & Freedman 1998). For the reddening, two values were checked:  $E(B-V) = 0.03$ , which was derived by SMH02 for the sample of the Inner Disk, using Strömberg photometry, and  $E(B-V) = 0.06$ , a mean value for the whole disk (Bessell 1991). We adopted CaT metallicities from SMH as our initial guesses and reported them in the  $[\text{Fe}/\text{H}]_{\text{CaT}}$  column of Table 2.

We have derived temperatures from V–I, V–K and J–K colors. We have found some trends when comparing temperatures from different colors:  $T_{\text{eff}}(V-I)$  is 65K hotter than  $T_{\text{eff}}(V-K)$  in the mean, with  $\sigma=59\text{K}$ ;  $T_{\text{eff}}(J-K)$  is 21K hotter than  $T_{\text{eff}}(V-K)$  and shows a highly dispersed relation, with  $\sigma=118\text{K}$  (these numbers vary only slightly when choosing

a reddening of  $E(B-V)=0.06$  or  $0.03$ ). As initial values of our stellar temperatures we have chosen to use a weighted mean of the estimates from  $V-I$  and  $V-K$ , omitting the less sensitive  $J-K$  color. We assign higher weight to the more temperature-sensitive ( $V-K$ ), according to the following expression:

$$T_{\text{eff}} = (T_{\text{eff}}(V - I) + 2 \times T_{\text{eff}}(V - K))/3.$$

In Table 2 the inferred temperatures for the two values of reddening,  $T_{\text{photLow}}$  and  $T_{\text{phot}}$  for  $E(B-V) = 0.03$  and  $0.06$  respectively, are given.

### 3.2. Spectroscopic parameters

The final stellar parameters used for the abundance determination of the sample stars were derived spectroscopically using abundances derived from the equivalent widths (EW) of iron lines. Although 67 stars were observed, 8 of them have one or two setups with low S/N, compromising the determination of stellar parameters. These stars have not been included in the abundance analysis. Due to low S/N ratios, the H13 setup has not been used for the following stars: RGB\_601, RGB\_646, RGB\_672, RGB\_699, RGB\_705, RGB\_710, RGB\_720, RGB\_731, RGB\_748, RGB\_756, RGB\_773 and RGB\_775; and for RGB\_666 the H11 setup has been discarded. We have estimated the stellar parameters as follows: effective temperatures are calculated by requiring no slope in the  $A(\text{Fe I})$  vs.  $\chi_{exc}$  (excitation potential) plot ( $\chi_{exc}$  is the excitation potential of the line); microturbulent velocities,  $V_t$ , are derived demanding that lines of different EW give the same iron abundance, also checking for no slope in the  $[\text{Fe/H}]$  vs.  $\log(W/\lambda)$  plot (iron abundance vs. the reduced equivalent width); and surface gravities are determined by forcing the agreement between Fe I and Fe II iron abundances (within the accuracy of the abundance determination of Fe II). For the temperature and surface gravity ranges covered by our current sample of stars,  $T_{\text{eff}}$  and  $\log g$  determinations are well correlated and the calculation of stellar parameters is made iteratively. In Fig. 2 we show an example of the excitation equilibrium calculation for RGB\_625, and in Fig. 3, the  $[\text{Fe/H}]$  vs.  $\lambda$  with the  $\log(W/\lambda)$  check, and the  $[\text{Fe/H}]$  vs. EW are given for RGB\_710. The spectroscopic and photometric parameters of all our stars are reported in Table 2, together with the barycentric radial velocities calculated from the spectra.

#### 3.2.1. Equivalent widths, line list and model atmospheres

The EW of the lines and the radial velocities (RV, in km/s, reported in Table 2) of the stars are computed using the program DAOSPEC<sup>2</sup> written by Stetson (Stetson and Pancino, in preparation). The line list and the atomic data were assembled from the

<sup>2</sup> The documentation and details about this program can be found in <http://cadwww.dao.nrc.ca/stetson/daospec/>.



literature and the oscillator strengths references are given in Table 3. DAOSPEC has already been used to measure the EW of spectra for different types of stars yielding reliable results (e.g. Pasquini et al. 2004, Barbuy et al. 2006, Sousa et al. 2006). We have made a study of the DAOSPEC EW estimations using GIRAFFE spectra. In the Appendix A we show a comparison of DAOSPEC EW with those made by hand using the Splot - Iraf task for six of our sample stars. We have found a very good agreement between the two methods for the analysis of the GIRAFFE spectra within the expected uncertainties.

MARCS 1D plane-parallel atmospheres models (Gustafsson et al. 1975, Plez et al. 1992, Gustafsson et al. 2003) were kindly provided by B. Plez (private communication).

### 3.2.2. Comparison with UVES analysis

In a previous observing run (066.B-0331), we obtained UVES spectra (in slit mode) for one of our sample stars, RGB\_666. UVES is an echelle spectrograph also mounted on the VLT Kueyen telescope with a higher resolving power:  $R = 45000$  (with a slit of  $1''$ ) and a much wider wavelength coverage (in the case of our chosen set-up, 4800-6800Å), and therefore with a better performance to derive equivalent widths. We have used this spectrum to evaluate DAOSPEC performance to derive EW from low resolution spectra. In Fig. 4, equivalent widths derived with DAOSPEC from UVES spectra from 5800 to 6800Å are compared to those measured also by this program on the GIRAFFE spectra of the same star using the same line list. In the top of the plot, the mean differences between analyses are given together with the dispersion and the number of lines used (lines of all elements are plotted in this comparison). We can see from this plot that GIRAFFE EW are only slightly higher than UVES EW. Such a difference is probably due to a better definition of the continuum for the UVES spectra, as well as the increased blending at the lower resolution of GIRAFFE. Using the EW of this figure, we have inferred the stellar parameters for UVES to compare the analysis from both spectrographs. We have found that the stellar parameters are almost identical to those given for RGB\_666 in Table 2, except for  $V_t$  for which we have found  $V_t = 1.8 \text{ kms}^{-1}$  (a difference of  $\Delta V_t = +0.1 \text{ kms}^{-1}$ ). Comparing the results from the two spectrographs, we have:  $[\text{FeI}/\text{H}]_{\text{UVES}} - [\text{FeI}/\text{H}]_{\text{GIRAFFE}} = -0.11 \text{ dex}$  and  $[\text{FeII}/\text{H}]_{\text{UVES}} - [\text{FeII}/\text{H}]_{\text{GIRAFFE}} = 0.00 \text{ dex}$ . Therefore it is possible that a systematic uncertainty of  $[\text{Fe}/\text{H}] \sim 0.1 \text{ dex}$  may be present in the following abundance analysis, although robust statements on this uncertainty would require better statistics. Let us further note that this 0.1 dex difference is within the errorbar that we quote for our GIRAFFE metallicities.

### 3.3. Behavior of stellar parameters

We found good agreement between spectroscopic and photometric temperatures. Our spectroscopic temperatures are hotter than photometric temperatures derived using the low reddening value,  $T_{\text{photLow}}$ , by 113 K, with  $\sigma=91\text{K}$ , and by 54K than  $T_{\text{phot}}$  (higher reddening value) with  $\sigma=64\text{K}$ . An interesting result is depicted in Fig. 5 where we compare the spectroscopic temperatures  $T_{\text{eff}}(\text{spec})$  with those derived from colors,  $T_{\text{eff}}(\text{V-I})$  and  $T_{\text{eff}}(\text{V-K})$ , and from the equation given in Sect. 3.1.1,  $T_{\text{eff}}(\text{phot})$ , for both values of reddening ( $E(\text{B-V})=0.06$  in the upper panels, and  $E(\text{B-V})=0.03$  in the lower panels). This figure shows that photometric temperatures inferred using  $E(\text{B-V}) = 0.06$  are in much better agreement with spectroscopic temperatures than those derived with the lower  $E(\text{B-V})$ . Provided that the photometric temperatures and the excitation temperature scale show a good agreement, this could indicate that  $E(\text{B-V})=0.06$  is a better reddening value for this region.

On average, spectroscopic surface gravities are lower than the photometric estimates by  $\Delta(\log g_{\text{spec}} - \log g_{\text{phot}}) = -0.38$  dex, as might be expected if NLTE overionization effects are at work (Korn et al. 2003). This systematic effect in  $\log g$  corresponds to a 0.2 dex difference between FeI and FeII.

The metallicities that we derive differ on average from those derived from the CaT by  $\Delta([\text{Fe}/\text{H}]_{\text{CaT}} - [\text{Fe}/\text{H}]_{\text{spec}}) = +0.13$  dex with  $\sigma = 0.27$  dex. In fact, most of this effect comes from the high-metallicity end of the sample: for  $[\text{Fe}/\text{H}]_{\text{CaT}} > -0.6$  dex, CaT seems to overestimate the metallicity systematically by 0.27 dex ( $\sigma = 0.19$  dex), whereas for the metal-poor end of the sample, there is almost no systematic effect ( $\Delta[\text{Fe}/\text{H}]_{\text{CaT}} - [\text{Fe}/\text{H}]_{\text{spec}}) = -0.04$  dex with  $\sigma = 0.24$  dex.

Finally, in Fig. 6, abundance ratios of different species,  $[\text{Cr}/\text{Fe}]$ ,  $[\text{Ni}/\text{Fe}]$  and  $[\text{V}/\text{Fe}]$ , against temperatures are plotted in order to check the quality of the spectroscopic temperatures. As can be seen from this picture, there is no trend of the abundances of the elements with temperature, which means that our temperatures are well defined. Our final sample comprises 59 red giant stars within  $-1.7 < [\text{Fe}/\text{H}] < -0.30$  dex and temperatures ranging from 3900 K to 4500 K.

## 4. Abundance determination

We have selected a list of lines covering the chosen setups in order to sample as much as possible the most important elements: iron-peak, neutron-capture and  $\alpha$  elements. Abundances are derived from EW measurements for eight elements (in parenthesis the average number of lines used in the analysis): Fe (45), Ni (7), Cr (4), V (11), Si (3), Ca (10), Ti (7) and Na (3). We have also derived abundances by using line synthesis for nine elements (in parenthesis the lines used in the synthesis): O ([O I] 6300Å); Mg I (5711 Å), Co I (5647 Å), Cu I (5782 Å), Sc II (5657 Å), La II (6320 Å), Y II (6435 Å), Ba II

(6496 Å), and Zr I (6134 Å). The code used for the abundance analysis was developed by Monique Spite (1967) and has been improved over the years. We note that both model atmospheres and the line synthesis program are in spherical geometry, so errors due to geometry inconsistencies are minimized (Heiter & Eriksson 2006). For the synthesis of the [O I] line in 6300.311 Å, we have taken into account the blend with Ni I 6300.336 Å (line data from Allende Prieto 2001), but no difference have been detected between results with or without such blend. Hyperfine structures (HFS) are taken into account for the following elements (the line sources are given in parenthesis): Ba II (Rutten 1978, and the isotopic solar mix following McWilliam 1998); La II (Lawler et al. 2001 with log gf from Bord et al. 1996); Cu (Biehl 1976), and Co I and Sc II (Prochaska et al. 2000). In Fig. 7 the fitting procedure is shown for the Y I 6435 Å line in RGB\_752 and the La II line 6320 Å in RGB\_690. Abundances are given relative to solar abundances of Grevesse & Sauval (2000). Atomic lines for the synthesis have been chosen according to the quality of the synthetic fit in the Solar Flux Atlas of Kurucz et al. (1984). In Tables 4 to 7 the derived abundances are given.

Errors in the derived abundances have three main sources: the uncertainties in the stellar parameters, the uncertainties in the measurements of the EW (or spectrum synthesis fitting) and the uncertainties on the physical data of the lines (mainly log gf). The errors due to stellar parameters uncertainties have been chosen as the maximum range each parameter could change not to give unrealistic models atmospheres. The errors  $\delta([X/Fe])_{\text{model}}$ , are given in Table 8, assuming the following uncertainties in each of the stellar parameters:  $\Delta(T_{\text{eff}}) = \pm 100\text{K}$ ,  $\Delta(\log g) = \pm 0.4 \text{ dex}$ ,  $\Delta(V_t) = \pm 0.2 \text{ km/s}$  and  $\Delta([Fe/H]) = \pm 0.15 \text{ dex}$ .

Errors in the EW measurement are computed by DAOSPEC during the fitting procedure, then propagated into an abundance uncertainty for each line, and then combined into an abundance error on the mean abundance for each element ( $\delta_{\text{DAOSPEC}}$ ). Errors due to the combined uncertainties on the line data and line measurement are reflected in the abundance dispersion observed for each element, provided that the number of lines is large enough to measure this dispersion in a robust way ( $N \geq 3$ ). We therefore combined these error estimates in a conservative way as given below:

$$\begin{aligned} N_X < 3: \delta([X/H]) &= \delta_{\text{DAOSPEC}}, \\ N_X \geq 3: \delta([X/H]) &= \text{Max}(\delta_{\text{DAOSPEC}}, \frac{\sigma(X)}{\sqrt{N_X}}) \end{aligned} \quad (1)$$

where  $N_X$  is the number of lines of the element X and  $\sigma(X)$  the dispersion among lines.

These errors are calculated for each element and given in Tables 4 to 6 together with the abundances derived from the EW. For elements measured by synthesis spectrum fitting, an error estimate has been carried out of the typical abundance change for which two different synthetic spectra (i.e. computed with two slightly different abundances) still fit satisfactorily the same line. On average, these values are the following for each

element:  $\delta[\text{Zr}/\text{H}] = 0.15$  dex;  $\delta[\text{Y}/\text{H}] = 0.15$  dex;  $\delta[\text{La}/\text{H}] = 0.20$  dex;  $\delta[\text{Ba}/\text{H}] = 0.25$  dex;  $\delta[\text{Co}/\text{H}] = 0.10$  dex;  $\delta[\text{Cu}/\text{H}] = 0.20$  dex;  $\delta[\text{Sc}/\text{H}] = 0.10$  dex;  $\delta[\text{Mg}/\text{H}] = 0.15$  dex and  $\delta[\text{O}/\text{H}] = 0.20$  dex. For the error bars reported in our abundance plots (always shown in the lower left corner of Figs. 8-12) we have adopted two error sources. The first, due to stellar parameter uncertainties (leftmost side of the plots), comes directly from Table 8, whereas the second (more to the right side) represents the error associated with the abundance analysis. For those abundances derived from the EW, this is the mean error of Tables 4,5, and 6, and for those elements with abundances derived from spectrum synthesis, it is the value described earlier on in this Section.

## 5. Abundance Distributions and comparison to Galactic samples

In Figs. 8 to 12 we depict the elemental distributions for the  $\alpha$ -elements, the iron-peak group, Na, Sc, Cu and  $s$ -elements for our stars compared to different samples of the Galaxy and the LMC. Our data are represented as dots. The references of the disk are: Fulbright 2000 (crosses); Reddy et al. 2003 (open squares); Allende Prieto et al. 2004 (open stars); Prochaska et al. 2000 (open triangles); Burris et al. 2000 (stars - only for the heavy-elements plots); Johnson & Bolte 2002 (open triangles - only for the heavy-elements plots); Simmerer et al. 2004 (open hexagons); Nissen & Shuster 1997 (asterisks, only stars with low  $[\alpha/\text{Fe}]$  ratios); Nissen et al. 2000 (asterisks - Sc abundances for the low- $\alpha$  stars); and Bensby et al. 2004 (open squares - only for the oxygen plot). LMC globular clusters (GC) stars from Hill et al. (2000, hereafter HI00) for O, and Hill (2004 hereafter HI04) for Na, Mg, Ca and Si are plotted as downward-pointing, open triangles; LMC GC stars from JIS06 are represented as open diamonds; field LMC red giants of SM02 are depicted as open pentagons. Error bars as described in Sect.4.0.1 are shown in the lower left side of the plots.

### 5.1. Ca, Si and Ti

In Fig. 8, the elemental distributions for Ca I, Si I, and Ti I are depicted. We have found that  $[\text{Si}/\text{Fe}]$  follows roughly the solar ratio with some scatter.  $[\text{Ca}/\text{Fe}]$  shows a slight decrease with metallicity. Compared to the distribution of the galactic halo, both silicon and calcium mean abundances are deficient by a factor of 3. Ti I ratios are also underabundant relative to galactic disk and galactic halo samples, and agree very well with the results of SM02, who derived titanium abundances from neutral lines for a sample of red giants from LMC disk. There is a hint of a decreasing trend of Ti abundances for higher metallicity stars, especially when SM02 datapoints are taken into account together with our sample. Compared to the LMC GC of H04, we have found that the star of our sample with metallicity similar to those of those of Hill et al. (2004) also has

similar  $[\text{Ca}/\text{Fe}]$  ratio. The JIS06 sample of LMC GC stars seems to overlap our  $[\text{Ca}/\text{Fe}]$  and  $[\text{Ti}/\text{Fe}]$  distributions, while their  $[\text{Si}/\text{Fe}]$  ratios are enhanced.

A very interesting result emerges when comparing our data with those of Nissen & Shuster 1997 (hereafter NS97, asterisks). NS97 discovered a sample of stars from the galactic halo with abnormal abundances: low  $[\alpha/\text{Fe}]$ ,  $[\text{Na}/\text{Fe}]$  and  $[\text{Ni}/\text{Fe}]$  ratios compared to “standard” halo stars. Such chemically peculiar or “low- $\alpha$ ” halo stars have an important role in elucidating the possible merging history of the galactic halo. Because of their chemical properties, they indicate that this group have formed in another stellar system that evolved separately, and which has been captured or ejected to the halo. Comparing our LMC distribution to the low- $\alpha$  stars, we have found that NS97 stars show a slightly enhanced mean  $\alpha$  abundance relative to our LMC stars.

Si, Ca and Ti are predicted to be produced in intermediate mass Type II SNe (SNe II) with a smaller contribution from Type Ia SNe (SNe Ia) (e.g. Tsujiomoto et al. 1995, Thielemann et al. 2002), while Fe is mostly produced by SNe Ia (e.g. Thielemann et al. 2001, Iwamoto et al. 1999). The low  $[\alpha/\text{Fe}]$  ratios observed indicate that SNe Ia have contributed more to the ISM content in the past than the SNe II.

## 5.2. Mg, O, Na and Sc

In Fig. 9, abundance ratios are given for O, Mg, Sc and Na. Nucleosynthetic predictions attribute the main source of O, Mg and Na to high-mass stars, with  $M > 25 M_{\odot}$ , which explode as SNe II (Woosley & Weaver 1995, hereafter WW95), with Na production controlled by the neutron excess. Although WW95 have attributed the origin of Sc to SNe II, the main source of Sc production is still unclear (e.g. McWilliam 1997, Nissen et al. 2000).

As can be seen in the upper panel of Fig. 9, oxygen ratios fall in the lower envelope of the galactic halo and disk distributions. For higher metallicities, it shows a faster decline with metallicity compared to stars from the galactic disk. In the second plot we see that the  $[\text{Mg}/\text{Fe}]$  ratios for the LMC Inner Disk overlap those of the Galaxy, but with smaller mean values. In contrast, Na and Sc behaviors are similar to those of the  $\alpha$ -elements Ti, and Si. Both elements are deficient and show smaller values for higher metallicities, while for the metal-poor tail, a match to the Galactic samples is observed. From this figure we see that the different LMC samples agree very well for all elements, Mg, O, Na and Sc, even the LMC globular clusters of H00, H04 and JIS06. A few stars in the NS00 sample of low- $\alpha$  stars show small  $[\text{Sc}/\text{Fe}]$  ratios and overlap our sample, but most of them show solar  $[\text{Sc}/\text{Fe}]$  values, higher than in our LMC sample. Sodium abundances in NS97 sample are similar to our values, although with a higher mean abundance. It is important to notice that sodium abundances in giants are still uncertain. Pasquini et al. (2004) found that  $[\text{Na}/\text{Fe}]$  ratios in giant stars are slightly higher than those from

dwarf stars in the same cluster. High  $[\text{Na}/\text{Fe}]$  ratios were also inferred from giants in M67 (Tautvaišienė et al. 2000). But such results have not been confirmed in the reanalysis of  $[\text{Na}/\text{Fe}]$  in giants and dwarfs of M67 (Randich et al. 2006).

Nissen et al. (2000) also found that Sc behaves similarly to Na, showing lower  $[\text{Sc}/\text{Fe}]$  ratios in their low- $\alpha$  stars, suggesting a correlation among those elements. In order to test the hypothesis of a correlation among Na and  $\alpha$ -elements, and Sc and  $\alpha$ -elements we have applied a statistical test to check for the existence and significance of such correlation, calculating the linear correlation coefficient, which varies from 1 or -1 (maximum correlation or anti-correlation) to 0 (no correlation). We have found that the correlations are weak: for Na-Ca, a correlation coefficient  $\phi = -0.06$  is found, and for Sc-Ca,  $\phi = 0.39$ .

### 5.3. Iron-peak elements

Abundance distributions for the iron-peak elements are shown in Fig. 10. The iron-peak elements Co, Ni and Cr display a very distinct pattern in the LMC Inner Disk stars, with underabundant values compared to the Galactic distributions and many subsolar ratios.  $[\text{Co}/\text{Fe}]$ ,  $[\text{Cr}/\text{Fe}]$  and  $[\text{Ni}/\text{Fe}]$  show a flat trend for most of the metallicity range, with mean abundances of  $\sim -0.18$  dex for Cr,  $\sim -0.24$  for Ni, and  $\sim -0.14$  dex for Co. The  $[\text{V}/\text{Fe}]$  ratios are similar to the galactic halo and disk patterns and track the solar value, with a group of stars showing smaller values. Results from the LMC GC of JIS06 seem to agree with our samples for Co, Ni and Cr. Vanadium in their sample shows an offset, with abundance ratios corresponding to the stars with smaller values in our sample. NS97 low- $\alpha$  stars overlap our sample for Ni and Cr, but lie in the high abundance envelope of the distributions.

According to nucleosynthetic predictions, iron-peak elements are mainly produced in SNe Ia (Iwamoto 1999, Travaglio et al. 2005): while each SN Ia produces  $\approx 0.8 M_{\odot}$  of the solar iron-peak elements, SN II produce  $\approx 0.1 M_{\odot}$  each (Timmes et al. 2003). The difference in the distributions from one environment to the other are an evidence that the production factors for each iron-peak element are not the same in the different types of SNe and depend on the SFH of the parent population. This will be further discussed in Sect. 7.

### 5.4. Copper

In Fig. 11 we show the plot for Cu. We have found that in the Inner Disk LMC stars, the copper distribution is flat, with a mean value of  $[\text{Cu}/\text{Fe}] = -0.68$  dex. Comparing to the Galaxy, there is an overlap between the LMC and Halo stars at the metal-poor end ( $[\text{Fe}/\text{H}] < -1.3$  dex); for the higher metallicity range, the distributions diverge, with LMC stars showing a clear underabundance with respect to the Galactic Disk. JIS06 also found an offset in their  $[\text{Cu}/\text{Fe}]$ , compatible to our abundance ratios.

Although originally associated with the iron-peak elements, the origin of copper is still much-debated (e.g. Bisterzo et al. 2004, Cunha et al. 2004, Mishenina et al. 2002). Sometimes its main source is attributed to SNe Ia (Matteucci et al. 1993, Cunha et al. 2002, Mishenina et al. 2002) and sometimes to SNe II, particularly to a metallicity dependent mechanism (Bisterzo et al. 2004; McWilliam & Smecker-Hane 2005). If the elemental behavior of the present sample, with low  $[\alpha/\text{Fe}]$ , low [iron-peak/Fe] ratios, is due to a higher contribution from SNe Ia, the overall low [Cu/Fe] pattern indicates that thermonuclear supernovae cannot be the main source of Cu production.

### 5.5. *s*-process elements

We have found interesting elemental distributions for the *s*-process elements for our sample stars (Fig. 12). While the light *s*-process elements (hereafter *ls*: elements made by the *s*-process with atomic number lower than  $\sim 45$ ) Zr and Y, show subsolar ratios with mean abundances the heavy *s*-process elements (hereafter *hs*: elements made by the *s*-process with atomic number higher than  $\sim 50$ ) La and Ba show supersolar values with enhanced pattern compared to those of the Galaxy. The underabundance of *ls* elements is quite strong,  $[\text{Y}/\text{Fe}] = -0.33$  dex and  $[\text{Zr}/\text{Fe}] = -0.48$  dex, and Zr shows a hint of decreasing with increasing metallicities. Of the *hs* elements, Ba has a peculiar behavior with a high value for one metal-poor star ( $[\text{Fe}/\text{H}] < -1.4$  dex), mild enhancements until  $[\text{Fe}/\text{H}] \sim -1.15$  dex, increasing again towards higher metallicities. La shows no trend with metallicity, with mild enhancements everywhere. One star, RGB\_1118, has particularly high La and Ba abundances ( $[\text{Ba}/\text{Fe}]$  and  $[\text{La}/\text{Fe}] \geq +1.0$  dex) and could be a star enriched in *s*-process elements (via mass-transfer from a former AGB companion), although it is not possible from our present data to discriminate between enhancements of *s*-process or *r*-process elements. The *s*-process elements in JIS06 sample are different when compared to our results. While they have found no offset for the *ls* elements compared to the galactic distribution, showing therefore a higher abundance compared to our stars, their *hs* elements (Ba and La) are less enhanced than ours. Comparing NS97 low- $\alpha$  stars with our sample, we find that these stars show abundances nearer those of normal disk stars for Ba and Y than the LMC stars.

The *hs/ls* ratios are high, showing large scatter, with a mean value of  $[\text{hs}/\text{ls}] = +0.77$  dex, as can be seen in Fig. 13. This is very different from what is observed for the galactic halo and disk stars, which fall around -0.2 to +0.2 dex (e.g. Pagel & Tautvaišienė 1997; Travaglio et al. 2004). A slow increasing trend with metallicity is observed.

High abundances of elements heavier than Zr were also derived for LMC and SMC supergiants (Russell & Bessell 1989; Spite et al. 1993; Hill et al. 1995). Hill et al. (1995) for example, found that the light *s*-elements Zr and Y show solar composition in LMC supergiants while heavier *s*-elements (Ba, La, Nd) as well as the *r*-process element Eu are

enhanced by +0.30 dex. As discussed by these authors, the overabundance of the heavier  $s$ -process and  $r$ -process elements seems to be a characteristic of the Magellanic Clouds, and indicate a particular evolution of that galactic system, although no satisfactory explanation was proposed for it.

In order to evaluate the  $r$ -process and  $s$ -process contributions within our sample we analysed the  $r$ -process content of one of our sample stars for which we have UVES spectra that cover the Eu  $\lambda$  6645 Å line. Eu and Ba abundances were derived from these spectra in the same way as was done for GIRAFFE spectra. For RGB\_666 we find respectively  $[\text{Ba}/\text{Fe}] = +0.52$ , and  $[\text{Eu}/\text{Fe}] = +0.40$  dex. The corresponding  $[\text{Ba}/\text{Eu}]$  ratio of 0.12 (to be compared with the solar  $r$ -process  $[\text{Ba}/\text{Eu}] = -0.55$  and the solar  $s$ -process  $[\text{Ba}/\text{Fe}] = +1.55$ , following Arlandini et al. 1999), indicate that this star contains a significant  $r$ -process contribution at a value close to the solar  $s/r$  mix at intermediate metallicities (RGB\_666:  $[\text{Fe}/\text{H}] = -1.10$ ).

A high content of  $r$ -process elements seems to be in contradiction with the observed low  $[\alpha/\text{Fe}]$  ratios (both being produced in massive stars). More data on Eu abundances are needed to confirm this high content of  $r$ -process elements, and in particular, the trend of the  $s/r$  fraction (traced by  $[\text{Ba}/\text{Eu}]$ ) as a function of metallicity will help to constrain the source of the high content of heavy  $s$ -process elements in the LMC disk. We intend to tackle this issue in the two other fields (Bar and Outer Disk) of our LMC program, since one of the MEDUSA wavelength ranges covers the Eu line for these fields.

### 5.5.1. The NaMg, NaNi relations

In the paper by NS97 the authors found a correlation between Na and Ni for their halo stars (both “normal” and “low- $\alpha$ ” stars). Such correlation has been confirmed for a group of stars in the Dwarf Spheroidal Galaxies (Shetrone et al. 2003, SH03, Tolstoy et al. 2003, TO03, Venn et al. 2004). To evaluate this trend, we plot in Fig. 14 the  $[\text{Ni}/\text{Fe}]$  vs.  $[\text{Na}/\text{Fe}]$  relation for our sample stars (dots) together with NS97 low- $\alpha$  stars. We see that the LMC stars also show a correlation between Na and Ni, although with a flatter pattern than the increasing trend observed for the NS97 sample. According to Tsujimoto et al. (1995), Ni can be produced in SNe Ia without Na production; therefore, a higher contribution from SNe Ia would flatten the NaNi relation<sup>3</sup> (Venn et al. 2004) and could explain the behavior of the LMC stars. In Fig. 14 we also analyze the correlation between Na and Mg and we find decreasing  $[\text{Na}/\text{Mg}]$  ratios for increasing  $[\text{Mg}/\text{H}]$  ratios. The NS97 low- $\alpha$  stars seem a continuation of the observed trend.

---

<sup>3</sup> however Travaglio et al. 2005 found that some Na and Mg are also produced in SNe Ia



## 6. Comparison to the Dwarf Spheroidal Galaxies

In Figs. 15 and 16 we show a comparison of the chemical distributions of our LMC sample to those of the dSph galaxies of Shetrone et al. (2003) and Tolstoy et al. (2003), and the Sagittarius dwarf galaxy (Sgr) of Bonifacio et al. (2004) and Sbordone et al. (2007). The elemental distributions of most dSph galaxies are more concentrated in the metallicity range for which we have the lowest number of stars,  $[\text{Fe}/\text{H}] < -1.2$ , so the present analysis is not ideal. In Fig. 15 the distributions for the  $\alpha$ -elements Ca, Ti and Si and for Cu are depicted (the description of the different symbols are given in the figure captions). As can be seen from these figures, and observed for also for O, Mg, Na and Sc, there is an overlap among the LMC abundance ratios and those of the dSph galaxies. The same occurs for the iron-peak elements Cr, V and Ni and for Cu (with the exception of Fornax, which shows higher values for Cu). Particularly, the agreement among our data and those of the Sagittarius dwarf galaxy is very good, except that this galaxy shows  $[\text{Ti}/\text{Fe}]$  and  $[\text{Mg}/\text{Fe}]$  ratios slightly underabundant relative to our values.

For the *s*-process elements, depicted in Fig. 16, the dSph galaxies show enhanced *hs* and deficient *ls* compared to the Galactic behavior, although the general pattern is less discrepant than that showed by the LMC inner disk stars, except for Sgr, which shows striking similar ratios when compared to our data. Fornax has a more metal-rich star (Fnx21) with high *s* content, which may be an *s*-enriched star. The  $[\text{Ba}/\text{Y}]$  ratios show a large offset relative to galactic samples, of the same order magnitude we have found. Venn et al. (2004) attribute such offset to primary *s*-process production by low-metallicity AGB stars.

The very similar elemental distributions of the Sgr galaxy indicate that this galaxy must have been very similar to LMC, i.e., with a higher mass content, which may be nowadays hidden in streams and/or dynamically mixed to the Galaxy.

## 7. Discussion

It is an amazing opportunity to have so much data on the amount of various elements of stars in an external galaxy. With this unique dataset, we can now explore in more detail the SFH and better understand the evolution of the LMC disk. The overall low  $[\text{X}/\text{Fe}]$  ratios indicate that such stars have undergone a global process which is different from that experienced by the average halo and disk stars in the Galaxy. In this section we discuss the possible explanations for such behavior.

We have found an overall low abundance pattern for the  $\alpha$ -elements, in agreement with many previous works with stars in this galaxy (Sect. 1). The heavy *s*-elements show an enhancement relative to the Galactic disk distributions, as inferred before for supergiants and red giants in the LMC. New results from the present work include low light-*s* abundance ratios ( $[\text{Y}/\text{Fe}]$  and  $[\text{Zr}/\text{Fe}]$ ), with most of the stars showing subsolar

values, and an unexpected offset for the iron-peak elements Ni, Cr and Co, and in some stars, also for V. Na and Sc are deficient with many subsolar ratios relative to iron, and copper shows a very low abundance in all stars from the present sample, with mean  $[\text{Cu}/\text{Fe}] \sim -0.7$  dex, and no trend with metallicity.

As seen in previous sections, small  $[\alpha/\text{Fe}]$  ratios have already been observed in other stellar systems such as the chemically peculiar halo stars (NS97, NS00), the dSph galaxies of the Local Group (Shetrone 2003, Tolstoy 2003), the Sagittarius galaxy (Smecker-Hane & McWilliam 2002, Bonifacio et al. 2004, Monaco et al. 2005, Sobordone et al. 2007), as in samples in the LMC (e.g. Hill et al. 2000, 2003; SM02, Garnett 2000, Korn et al. 2002). It is interesting to notice that the *s*-process trends in the dSph galaxies (enhanced *hs* and deficient *ls* ratios) are the same as for our stars. Correlations between abundances of iron-peak elements and  $\alpha$ -elements were observed also in other stellar systems. A pattern of slightly deficient Ni and Cr has been observed for the low- $\alpha$  stars of NS97. Bensby et al. (2003) found a correlation among the [iron-peak/Fe] and [Na/Fe] vs. [ $\alpha$ -elements/Fe] abundance ratios, i.e., slightly higher [Cr/Fe], [Ni/Fe] and [Na/Fe] ratios in thick disk stars with enhanced [ $\alpha$ -element/Fe] ratios (see their Fig. 13). Sbordone et al. (2007) found subsolar ratios for Na, Sc, Co, Ni and V in their analysis of the Sagittarius dwarf galaxy stars, which has also low  $[\alpha/\text{Fe}]$  ratios. Such behavior may tell us interesting details about the formation of these elements and give clues about low-mass galaxy formation.

Many interpretations have been given for the small  $[\alpha/\text{Fe}]$  ratios observed. One hypothesis is that the star formation (SF) developed slowly, in short bursts, followed by long quiescent periods without SF, during which the SNe Ia contaminated the ISM and increased the Fe content (e.g. Gilmore & Wyse 1991). Smaller SNe II/SNe Ia ratios, therefore a higher frequency of SNe Ia relative to SNe II, have also been invoked, within a bursty or continuous regime, and with or without galactic winds (e.g. Pagel & Tautvaišienė 1997, Smith et al. 2002); a steepened IMF relative to that of the solar neighborhood has been proposed by Tsujimoto et al. (1995) and de Freitas Pacheco (1998), whereas alpha-enriched galactic winds, which would lower the [ $\alpha$ /Fe] content, have been suggested by Pilyugin (1996); and finally, a small (low-mass) star-formation event that would effectively truncate the IMF, yielding fewer high-mass SNe II than produced by normal SF events has been suggested (Tolstoy et al. 2003). To find explanations for the behavior of the iron-peak elements is more puzzling, since they are predicted to be basically produced in SNe Ia (e.g. Travaglio et al. 2005). A possible explanation is that the yields of the SNe Ia are metallicity dependent (Timmes et al. 2003).

The abundance distributions observed for the *hs* and the *ls* elements, with  $hs/ls=[\text{Ba}+\text{La}/\text{Y}+\text{Zr}]$ , are in agreement with the hypothesis that the *s*-process in AGB stars is metallicity dependent (Busso et al. 1999 and references therein; Busso et al. 2001; Abia et al. 2003, Travaglio et al. 2004). It has been noticed that, due to details of the nucleosynthesis of the *s*-process, *hs*-elements (e.g. Ba, La and Nd) are preferentially pro-

duced by metal-poor AGB stars compared to *ls* elements (e.g. Y, Zr and Sr), which are most efficiently produced at  $[\text{Fe}/\text{H}] \approx -0.1$  (e.g. Fig. 1 of Travaglio et al. 2004). If the SF is slow, low-metallicity AGB stars have enough time to contaminate the ISM, leaving noticeable chemical signatures for the next generations.

Nevertheless, Venn et al. (2004) discuss the possibility that the abundances of these elements (including Y) in dSph cannot be accounted for solely by the *s*-process, requiring a strong contribution from the *r*-process. Also, according to Richtler et al. (1989) and Russell & Dopita (1992), the most probable explanation for the high Ba and La abundances observed in the Magellanic Clouds is an additional *r*-process component. This would mean that *hs* and *ls* elements are produced in different rates by the *r*-process nucleosynthesis, probably in different sites. Therefore, the analysis of the behavior of the *s*-elements in the given metallicity range is complex and must take into account both the *r* and the *s* contributions.

### 7.1. Galaxy Formation and Evolution

One of the most debated themes about galaxy formation in the Universe under a  $\Lambda$ CDM hierarchical scenario concerns the problem of overprediction of galaxy counts at low-*z* and underprediction at high-*z* (Cimatti et al. 2002). One of the consequences for the Local Group is a larger number of small galaxies than is actually observed although the number of dwarf galaxies observed around the Milky Way and M31 has lately grown significantly (eg. Belokurov et al. 2007). According to these models, numerous merging and accretion events play an important role in the formation process of massive galaxies (e.g. Moore et al. 1999), although not all dark matter clumps are predicted to host star formation and thereby become visible galaxies (e.g. Bullock & Johnston 2005). The quest for signatures of possible accreted stars from nearby galaxies in the Galactic halo and disk have been carried out, without definite conclusions (NS97, NS00, Ivans et al. 2003, Venn et al. 2004). A careful inspection of the elemental distributions of the different Galactic components reveals a low dispersion in the abundance ratios at each metallicity bin and smooth transitions between them (see e.g. plots from Venn et al. 2004). This seems to indicate a different process: that the Galaxy, including the halo, has grown in a holistic way, rather than by many independent accreting events, even for the galactic halo (see Gilmore & Wyse 2004). Another possibility is that the merging events occurred very early in the building process of our Galaxy, involving mostly dark matter and primordial gas. Such observational features hint for a common history within the same environment rather than a mix of SFHs. The results from the present work strongly support this idea, showing that an LMC-like SFH results in a quite distinctive elemental pattern not seen in any galactic stellar population.

We have found that the elemental compositions of the LMC Inner Disk stars show a different pattern when compared to their galactic counterparts (if we exclude the low-alpha stars of NS97). This indicates that possible accreting events of LMC and LMC-like fragments (Bekki & Chiba 2005, Robertson et al. 2005), from which our Galactic halo could have been built, are unlikely, but strong conclusions are still not possible because more representative samples are needed, from both halo and LMC stars. However, we stress here that the stellar populations probed in the LMC are mostly intermediate age, and would not have been merged into a Milky Way halo or disk if the accretion of an LMC-like galaxy occurred early on ( $z > 1$ ). Strong conclusions concerning the possible early accretion of LMC-type systems therefore still await detailed analysis of the elemental abundances of representative samples of the oldest populations in the LMC. The elemental distributions of the LMC Inner Disk also hint for a different process of galaxy formation, showing that the galactic local environment is fundamental for the amount of various elements of its components.

## 8. Summary

In the present paper we report abundance ratios for a series of elements, including  $\alpha$ ,  $s$ - and iron-peak elements, Na, Sc and Cu for a sample of 59 RGB stars of the inner LMC disk. We have found a very different behavior for most of the elements relative to stars from the Galaxy with similar metallicity, hinting at a very different evolutionary history. On the other hand, there is a good overall agreement between the elemental distributions of our sample stars and previous results of the LMC GC and field stars of Hill et al. (2000, 2003), Smith et al. (2002) and Johnson et al. (2006). The main results are summarized as follows:

- $[\alpha/\text{Fe}]$  ratios show an overall deficient pattern relative to Galactic distributions, in agreement with a slower star-formation history in the LMC, leading to a stronger Type Ia supernovae influence. However, all  $\alpha$ -elements do not show the same degree of deficiency: while O/Fe and Mg/Fe are hardly different in the LMC and Milky-Way disks, Si, Ca and Ti are strongly underabundant. This illustrates that all  $\alpha$ -elements are not alike from the nucleosynthesis point of view
- Cu is strongly depleted with respect to iron,  $[\text{Cu}/\text{Fe}] \simeq -0.70$  dex, with no apparent trend with metallicity. This also hints at a strong contribution of Type Ia supernovae to the creation of copper
- the  $[\text{X}/\text{Fe}]$  deficiency of the  $\alpha$ -elements is also displayed by Na, Sc, and, in an unexpected behavior, by the iron-peak elements Ni, Cr and Co. The iron peak elements underabundances are not expected in any standard chemical evolution model (i.e. currently not predicted by SNe yields)

- we have found relationships between Na-Ni and Na-Mg, in agreement to those derived by Nissen & Schuster (1997) for a sample of low- $\alpha$  halo stars. As Na is predicted to be mainly produced by SNe II, together with O and Mg, a relationship Na-Mg is expected, although Na production is also controlled by the neutron excess during carbon burning in massive stars (Umeda et al. 2000). The Na-Ni relationship is also expected if Ni is also produced in SN II, with yields dependent on the neutron excess (Thielemann et al. 1990)
- heavy neutron capture elements fall into two well-defined groups: while high-mass *s*-process elements (Ba and La) present an enhanced pattern, low-mass *s*-process elements (Y and Zr) are deficient relative to the galactic samples. Such behavior has been observed before in LMC and SMC F supergiants and in dSph galaxy RGB stars. It could reflect a strong contribution of metal-poor AGB stars to the metal-enrichment of these systems, as low-metallicity AGB stars preferentially produce the heavier *s*-process elements over the lighter ones (see Travaglio et al. 2004 for the theoretical side and de Laverny et al. 2006 for the observation of low metallicity AGBs)
- we have derived Eu abundances for one of our intermediate-metallicity stars (RGB\_666: [Fe/H]=-1.10), and combined with the measured Ba abundance for this star, this enabled us to disentangle the respective *r*- and *s*-process contributions to heavy neutron-capture elements: this star contains a solar mix of *r*- and *s*-process elements. Although a single measurement is obviously not enough to conclude, we thereby confirm that the high abundances of *ls* elements observed at intermediate metallicity should be attributed to the *s*-process.

For the next two fields of our program (see Introduction) the wavelength range of the spectra covers a Eu line and a better evaluation of such contributions will be possible

- compared to the dSph galaxies, similar abundance ratios for almost all the elements have been derived, with slight enhancements of La, Ba, Na and Y, although the match in metallicity among our sample and the dSph samples is not ideal. LMC Inner Disk abundances of Ca, Si, Ti and Cu are also similar to those of the Sagittarius dwarf galaxy. The commonalities between the LMC inner disk population and the samples in dSph galaxies indicate that all these galaxies may have undergone similar SFH

The overall pattern of the elemental distributions for the LMC Inner Disk population can be explained by a higher contribution of Type Ia SNe, indicating that the build up of this population has been slower than that of the solar neighborhood stars. A higher contribution from metal-poor ABG stars is also proposed. The present results support the hypothesis that the elemental distributions of the stars are directly related to galaxy they pertain.

## References

- Abia, C., Domínguez, I., Gallino, R., Busso, M., Masera, S., Straniero, O., de Laverny, P., Plez, B., Isern, J. 2002, ApJ 579, 817
- Allende Prieto, C., Barklem, P. S., Lambert, D. L., Cunha, K. A&A 420, 183
- Barbuy, B., Zoccali, M., Ortolani, S., Momany, Y., Minniti, D., Hill, V., Renzini, A., Rich, R. M., Bica, E., Pasquini, L., Yadav, R. K. S. 2006, A&A 449, 349
- Belokurov, V., Zucker, D. B., Evans, N. W., et al. 2007, ApJ 654, 897
- Bensby, T., Feltzing, S., Lundstrom, I. 2003, A&A 410, 527
- Bensby, T., Feltzing, S., Lundstrom, I. 2004, A&A 415, 155
- Bessell, M.S., Castelli, F. & Plez, B. 1998, A&A 333, 231
- Bessell, M.S. 1991, A&A 242L, 17
- Biehl, D. 1976, Ph.D. Thesis, Kiel
- Bisterzo, S., Gallino, R., Pignatari, M., Pompeia, L., Cunha, K., Smith, V. 2004, MmSAI v.75, p.741
- Bonifacio, P., Sbordone, L., Marconi, L., Pasquini, L., Hill, V. 2004, A&A 414, 503
- Bord, D. J., Barisciano, L. P., Cowley, C. R. 1996, MNRAS, 278, 997
- Bullock, J.S. & Johnston, K.V. 2005, ApJ 635, 931
- Butcher, H. 1977 ApJ 216, 372
- Burris, D.L., Pilachowski, C.A., Armandroff, T.E., Sneden, C., Cowan, J.J., Roe, H. 2000, ApJ 544, 302
- Busso, M., Gallino, R., Wasserburg, G. J. 1999, ARA&A, 37, 239
- Busso, M., Gallino, R., Lambert, D.L., Travaglio, C., Smith, V.V. 2001, ApJ 557, 802
- Carpenter, J.M. 2001, AJ, 121, 2851
- Cayrel, R. 1988, in in IAU Symp. 132, The Impact of Very High S/N Spectroscopy on Stellar Physics, eds. G. Cayrel de Strobel & M. Spite (Dordrecht: Kluwer), 345
- Cayrel, R., Depagne, E., Spite, M., Hill, V., Spite, F., Franois, P., Plez, B., Beers, T., Primas, F., Andersen, J., Barbuy, B., Bonifacio, P., Molaro, P., Nordstrm, B. 2004, A&A 416, 1117
- Cimatti, A., Pozzetti, L., Mignoli, M., Daddi, E., Menci, N., Poli, F., Fontana, A., Renzini, A., Zamorani, G., Broadhurst, T., Cristiani, S., D'Odorico, S., Giallongo, E., Gilmozzi, R. 2002 A&A 391L, 1
- Cioni, M.-R., Girardi, L., Marigo, P., Habing, H.J. 2006, A&A 448, 77
- Cunha, K., Smith, V.V., Suntzeff, N.B., Norris, J.E., Da Costa, G.S., Plez, B. 2004, AJ 124, 379
- Da Costa, G. S. 1991, in IAU Symp 148, "The Magellanic Clouds", eds. R. Haynes and D. Milne, Kuwer: Dordrecht, p. 183
- Da Costa, G. S. 1999, in IAU Symp 190, "New Views on the Magellanic Clouds", eds. Y.-H Chu, N. Suntzeff, J. Hesser, D. Bohlender, ASP: San Francisco, p. 397
- de Laverny P., Abia C., Dominguez I., Plez B., Straniero O., Wahlin R., Eriksson K., Jørgensen U., 2006 A&A 446, 1107
- D'Onghia, E., & Lake, G., 2004 ApJ 612 628
- Dufton, P. L.; Smartt, S. J.; Lee, J. K. et al. 2006, A&A 2006, 457, 265
- de Freitas Pacheco, J.A. 1998, Aj 116, 1701
- de Vaucouleurs, G. 1980, PASP 92, 576

- Edvardsson, B., Andersen, J., Gustafsson, B., Lambert, D. L., Nissen, P. E., Tomkin, J. 1993, *A&A* 275, 101
- Evans, C. J.; Smartt, S. J.; Lee, J.-K.; Lennon, D. J. et al. 2005, *A&A* 437, 467
- Fernie, J.D. 1983, *PASP* 95, 782
- Fulbright, J. P. 2000, *AJ* 120 1841
- Garnett, D.R. 1999, in *IAU Symp. 190, New Views of the Magellanic Clouds*, eds. Y.-H. Chu, N. Suntzeff, J. Hesser, D. Bohlender, p.266
- Geha, M. C., Holtzman, J. A., Mould, J. R., et al. 1998, *AJ*, 115, 1045
- Gilmore G., Wyse R.F.G. 1991, *ApJ* 367, L55
- Gilmore G., Wyse R.F.G. 2004, astro-ph/0411714
- Grevesse, N., Sauval, A. J. 2000, in "Origin of Elements in the Solar System, Implications of Post-1957 Observations, Proc. of the International Symposium. Edited by O. Manuel. Boston/Dordrecht: Kluwer Academic/Plenum Publishers, p.261
- Gustafsson, B., Bell, R. A., Eriksson, K., Nordlund, A. 1975, *A&A* 42, 407
- Gustafsson, B., Edvardsson, B., Eriksson, K., Mizuno-Wiedner, M., Jørgensen, U. G., Plez, B. 2003, in "Stellar Atmosphere Modeling", ASP Conf. Proc. 288, Edited by I. Hubeny, D. Mihalas, and K. Werner, San Francisco, ASP, 331
- Hill, V., Andrievsky, S. Spite, M. 1995, *A&A* 293, 347
- Hill, V., & Spite, M. 1999, in "Galaxy Evolution: Connecting the Distant Universe with the Local Fossil Record", Proc. Coll. Obs. Paris-Meudon. Edited by M. Spite, Kluwer Academic Publishers, Dordrecht, p. 469.
- Hill, V., Francois, P., Spite, M., Primas, F., & Spite, F. 2000, *A&A* 364 L19
- Hill, V. 2004, in *Carnegie Observatories Astrophysics Series, Vol. 4: Origin and Evolution of the Elements*, ed. A. McWilliam and M. Rauch (Cambridge: Cambridge Univ. Press), p.205
- Holtzman, Jon A.; Gallagher, John S., III; Cole, Andrew A.; Mould, Jeremy R.; Grillmair, Carl J.; Ballester, Gilda E.; Burrows, Christopher J.; Clarke, John T.; Crisp, David; Evans, Robin W.; Griffiths, Richard E.; Hester, J. Jeff; Hoessel, John G.; Scowen, Paul A.; Stapelfeldt, Karl R.; Trauger, John T.; Watson, Alan M. 1999, *AJ* 118, 2262
- Hunter, I.; Dufton, P. L.; Smartt, S. J.; Ryans, R. S. I.; Evans, C. J.; Lennon, D. J.; Trundle, C.; Hubeny, I.; Lanz, T. 2007, *A&A* 466, 277
- Ivans, I.I., Sneden, C., James, C.R., Preston, G.W., Fulbright, J.P., Hflich, P.A., Carney, B.W., Wheeler, J.C. 2003, *ApJ* 592, 906
- Iwamoto, K., Brachwitz, F., Nomoto, K., Kishimoto, N., Umeda, H., Hix, W.R., Thielemann, F.-K. 1999, *ApJS* 125, 439
- Javiel, S. C.; Santiago, B. X.; Kerber, L. O. 2005, *A&A* 431, 73
- Johnson, J. & Bolte, M. 2002, *ApJ* 579, 616
- Johnson, J., Bolte, M., Hesser, J.E., Ivans, I.I. 2004, in *Carnegie Observatories Astrophysics Series, Vol. 4: Origin and Evolution of the Elements*, ed. A. McWilliam and M. Rauch, p. 29
- Korn, A. J., Keller S. C., Kaufer A., Langer N., Przybilla N., Stahl O., Wolf B. 2002, *A&A* 385, 143
- Korn, A. J., Shi J., Gehren, T., 2003, *A&A* 407, 691
- Kraft, R.P. Sneden, C., Langer, G.E. & Prosser, C.F. 1992, *AJ* 104, 645

- Kurucz, R.L., Furenlid, I., Brault, J. 1984, National Solar Observatory Atlas, Sunspot, New Mexico: National Solar Observatory, 1, 984
- Lawler, J. E., Bonvallet, G., Sneden, C. 2001, ApJ 556, 452
- Luck, R.E. & Lambert, D.L. 1992, ApJS 79, 303
- Madore, B. F., & Freedman, W. L. 1998, ApJ, 492, 110
- Matteucci, F., Raiteri, C.M., Busson, M., Gallino, R., & Gratton, R. 1993, A&A, 272, 421
- McWilliam, A. 1997, ARA&A 35, 503
- McWilliam, A. 1998, AJ 115, 1640
- McWilliam, A., Smecker-Hane, T. 2005, ApJ 622, 29
- Mishenina, T. V., Kovtyukh, V. V., Soubiran, C., Travaglio, C., & Busso, M. 2002, A&A, 396, 189
- Moore, B., Ghigna, S., Lake, G., Quinn, T., Stadel, J., & Tozzi, P. 1999, ApJ, 524, L19
- Nissen, P. E., Schuster, W. J. 1997, A&A 326, 752
- Nissen, P. E., Chen, Y. Q., Schuster, W. J., Zhao, G., 2000, A&A 353, 722
- Olszewski, E.W.; Suntzeff, N.B.; Mateo, M. 1996, ARA&A 34, 511
- Pagel, B. E. J., Tautvaišiene, G. 1997, MNRAS 288, 108
- Pasquini, L., Avila, G., Blecha, A. et al. 2002, The Messenger, 110, 1
- Pasquini, L., Randich, S., Zoccali, M., Hill, V., Charbonnel, C., Nordström, B. 2004, A&A 424, 951
- Pilyugin, L.S. 1996, A&A 310, 751
- Plez, B., Brett, J.M., Nordlund, A. 1992, A&A 256, 551
- Plez, B. 2000, Proc. IAU Symp. 177, 'The Carbon Star Phenomenon', Wing, R.F. ed., Kluwer Academic Publishers, Dordrecht, p.71
- Prochaska, J. X., Naumov, S. O., Carney, B. W., McWilliam, A., & Wolfe, A. M. 2000, AJ 120 2513
- Randich, S., Sestito, P., Primas, F., Pallavicini, R., Pasquini, L. 2006, A&A 450, 557
- Reddy, B. E., Tomkin, J., Lambert, D. L., & Allende Prieto, C. 2003, MNRAS 340, 304
- Richtler, T., Spite, M., Spite, F. 1989, A&A 225, 351
- Rolleston, W. R. J., Trundle, C., Dufton, P. L. 2002, A&A 396, 53
- Russell, S.C. & Bessell, M.S. 1989, ApJS 70, 865
- Russell, S.C. & Dopita, M.A. 1992, ApJ 384, 508
- Rutten, R.J., 1978, Solar Physics 56, 237
- Sarajedini, A. 1998, AJ 116, 38
- Sbordone, L., Bonifacio, P., Buonanno, R., Marconi, G., Monaco, L., Zaggia, S. 2007, 465, 815
- Shetrone, M. D., Venn, K. A., Tolstoy, E., Primas, F., Hill, V., & Kaufer, A. 2003, AJ, 125, 684
- Smecker-Hane, T.A., Cole, A.A., Gallagher, J.S.III, Stetson, P.B. 2002, SMH02, ApJ 566, 239
- Smecker-Hane T., Cole A., Mandushev, G.I., Bosler, T. L., Gallagher J., in press
- Smecker-Hane, T.A., Cole, A.A., Mandushev, G.I., Bosler, T.L., Gallagher, J.S. 2007, in preparation
- Smecker-Hane T., McWilliam, A. 2002, Proc. Symp. 'Cosmic Abundances as Records of Stellar Evolution and Nucleosynthesis in honor of David L. Lambert' ASP Conf. Series, Thomas G. Barnes III and Frank N. Bash eds., San Francisco, V. 336, 221



- Smith, V.V., Hinkle, K.H., Cunha, K., Plez, B., Lambert, D.L., Pilachowski, C.A., Barbuy, B., Melendez, J., Balachandran, S., Bessell, M.S., Geisler, D.P., Hesser, J.E., Winge, C. 2002, *AJ* 124, 3241
- Snedden, C., Gratton, R.G., Crocker, D.A. 1991, *A&A*, 246, 354
- Sousa, S. G.; Santos, N. C.; Israelian, G.; Mayor, M.; Monteiro, M. J. P. F. G. 2006, *A&A* 458, 873
- Spite, M. 1967, *Ann. d'Astrophys.*, 30, 21
- Spite, F., Barbuy, B., Spite, M. 1993, *A&A* 272, 116
- Subramaniam, A. 2004, *A&A* 425, 837
- Tautvaišiene, G., Edvardsson, B., Tuominen, I., Ilyin, I. 2000, *A&A*, 360, 499
- Thielemann, F.-K., Hashimoto M., Nomoto K. 1990, *ApJ* 349, 222
- Thielemann, F.-K., Brachwitz, F., Freiburghaus, C., Kolbe, E., Martinez-Pinedo, G., Rauscher, T., Rembges, F., Hix, W. R., Liebendrfel, M., Mezzacappa, A., Kratz, K.-L., Pfeiffer, B., Langanke, K., Nomoto, K., Rosswog, S., Schatz, H., Wiescher, W. 2001, *PPNP*, 46, 5
- Thielemann, F.-K., Argast, D., Brachwitz, F., Martinez-Pinedo, G., Rauscher, T., Liebendrfel, M., Mezzacappa, A., Hflich, P., Nomoto, K. 2002, *Ap&SS* 281, 25
- Timmes, F. X., Brown, Edward F., Truran, J. W. 2003, *ApJ* 590, 83L
- Tolstoy, E., Venn, K. A., Shetrone, M. D., Primas, F., Hill, V., Kaufer, A., & Szeifert, T. 2003, *AJ*, 125, 707
- Travaglio, C., Gallino, R., Arnone, E., Cowan, J., Jordan, F., Sneden, C. 2004, *ApJ* 601, 864
- Travaglio, C. Hillebrandt, W., Reinecke, M., Thielemann, F.-K, 2005, [astro-ph/0406281](https://arxiv.org/abs/astro-ph/0406281)
- Tsujimoto, T., Nomoto, K., Yoshii, Y., Hashimoto, M., Yanagida, S., Thielemann, F.-K. 1995, *MNRAS* 277, 945F
- Umeda, H., Nomoto, K., Nakamura, T 2000, in *The First Stars*, ed. A. Weiss, T. Abel, & V. Hill Heidelberg: Springer, 150
- van den Bergh, S. 1979, *ApJ* 230, 95
- van den Bergh, S. 1998, *ApJ* 507, L39
- van den Bergh, S. 1999, *IAU Simp.* 190, "New Views of the Magellanic Clouds", Y.-H. Chu, N. Suntzeff, J. Hesser, & D. Bohlender (Eds.)
- van der Marel, R.P., Cioni, M.-R. L. 2001, *AJ* 122, 1807
- Venn, K.A., Irwin, M., Shetrone, M.D., Tout, C.A., Hill, V., Tolstoy, E. 2004, *AJ* 128, 1177
- Westerlund, B. E. 1997, *The Magellanic Clouds* Cambridge: Cambridge Univ. Press)
- Woosley, S.E., Weaver, T.A. 1995, *ApJS* 101, 181

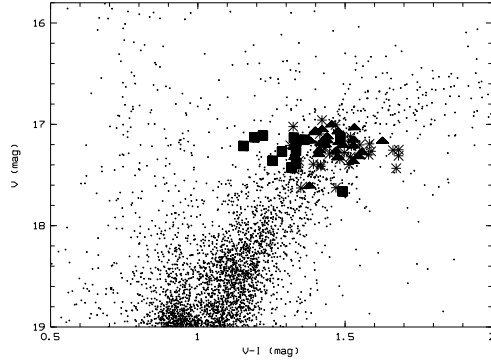


**Fig. 1.** V (V-I) color-magnitude diagram of the Disk region (following SMH02), with our sample stars overplotted: *asterisks* are stars with  $[\text{Fe}/\text{H}]_{CaT} \geq -0.5$  dex, *triangles*  $-1.0 \leq [\text{Fe}/\text{H}]_{CaT} < -0.5$  dex, *squares*  $[\text{Fe}/\text{H}]_{CaT} < -1.0$  dex.

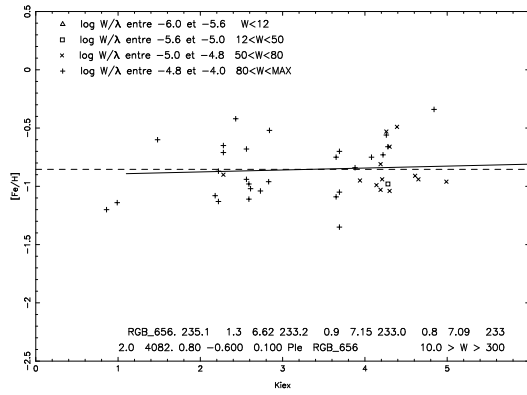


**Fig. 2.** Example of the temperature calculation for RGB\_625:  $[\text{Fe I}/\text{H}]$  vs.  $\chi_{exc}$ .

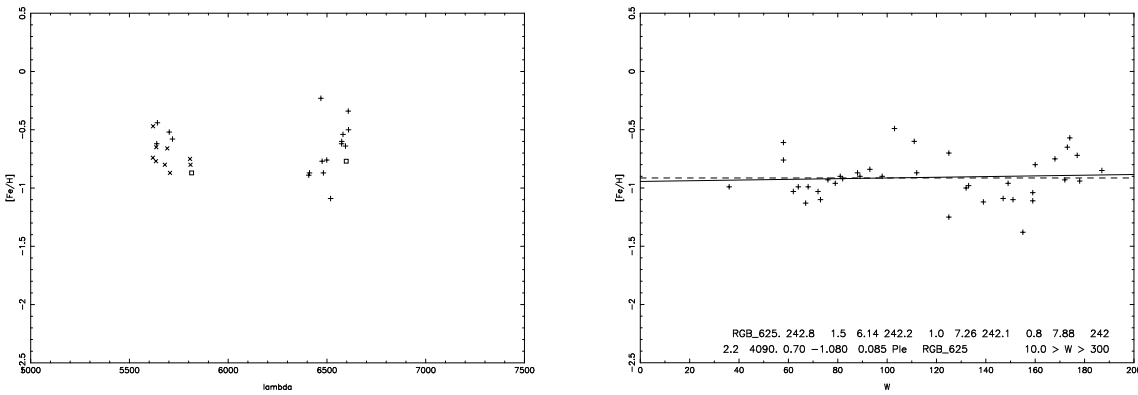


**Fig. 3.** Examples of microturbulence velocity calculation for RGB\_710:  $[\text{Fe I}/\text{H}]$  vs.  $\lambda$  (left); and  $[\text{Fe I}/\text{H}]$  vs. EW (right). The different values for the reduced EW in the left panel are given with different symbols: 1) squares:  $-5.6 \leq \log W/\lambda \leq -5.0$  and  $12 < W < 50$ ; 2) crosses:  $-4.8 \leq \log W/\lambda \leq -4.0$  and  $80 < W < 300$ ; and 3) times:  $-5.0 \leq \log W/\lambda \leq -4.8$   $50 < W < 80$ .

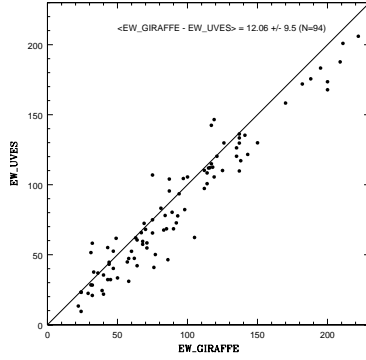


Fig. 4. Comparison between UVES and GIRAFFE spectra analyses for RGB\_666.

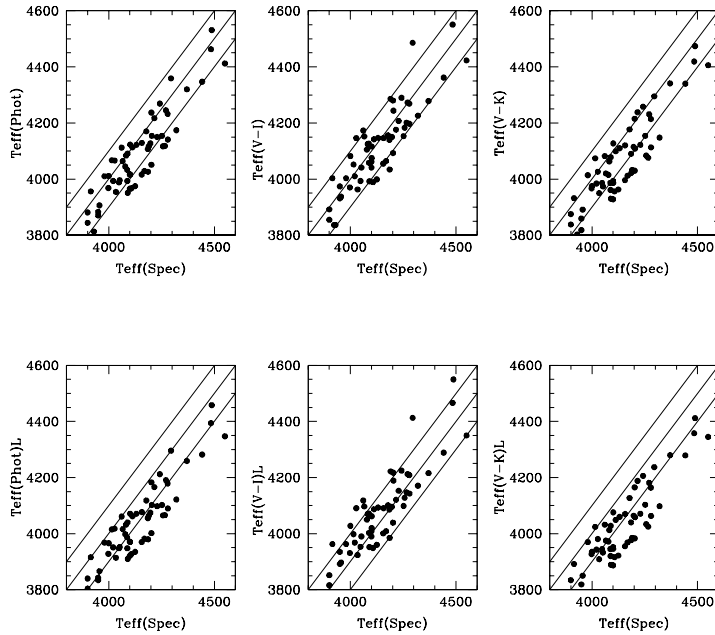
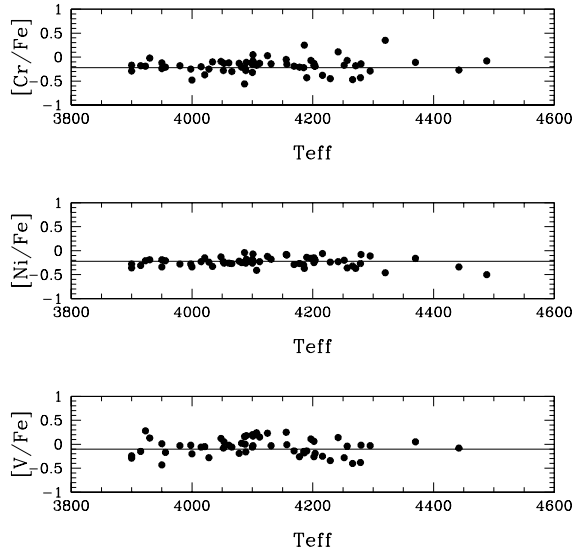
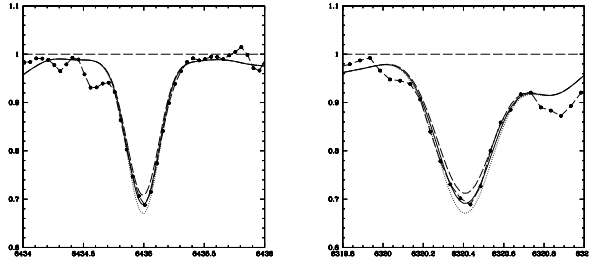


Fig. 5. Comparison between photometric and spectroscopic temperatures (see text). On the bottom plots, photometric temperatures are derived with  $E(B-V)=0.03$  (SMH02), while on the upper plots, photometric temperatures are derived with a higher reddening value,  $E(B-V)=0.06$  (Bessel 1991). Solid lines represent  $T_{\text{eff}(\text{spec})} = T_{\text{eff}(\text{phot})}$  and  $T_{\text{eff}(\text{spec})} = T_{\text{eff}(\text{phot})} \pm 100\text{K}$ .



**Fig. 6.** Abundance ratios against temperatures. From top to bottom:  $[\text{Cr}/\text{Fe}]$  vs.  $T_{\text{eff}}$ ,  $[\text{Ni}/\text{Fe}]$  vs.  $T_{\text{eff}}$  and  $[\text{V}/\text{Fe}]$  vs.  $T_{\text{eff}}$ .



**Fig. 7.** Example of the line synthesis procedure for the Y I and La II lines: left panel: Y I  $\lambda 6435\text{\AA}$  line fitting for RGB\_752; right panel: La II  $\lambda 6320\text{\AA}$  line fitting for RGB\_690. The black circles depict the observed spectra and the lines are the synthetic spectra. Abundances of the synthetic spectra are:  $[\text{Y}/\text{Fe}] = -0.55$  (dashed line),  $-0.45$  (continuous line - best fit),  $-0.25$  (dotted line); and  $[\text{La}/\text{Fe}] = 0.56$  (dashed line),  $0.66$  (continuous line - best fit), and  $0.76$  (dotted line).

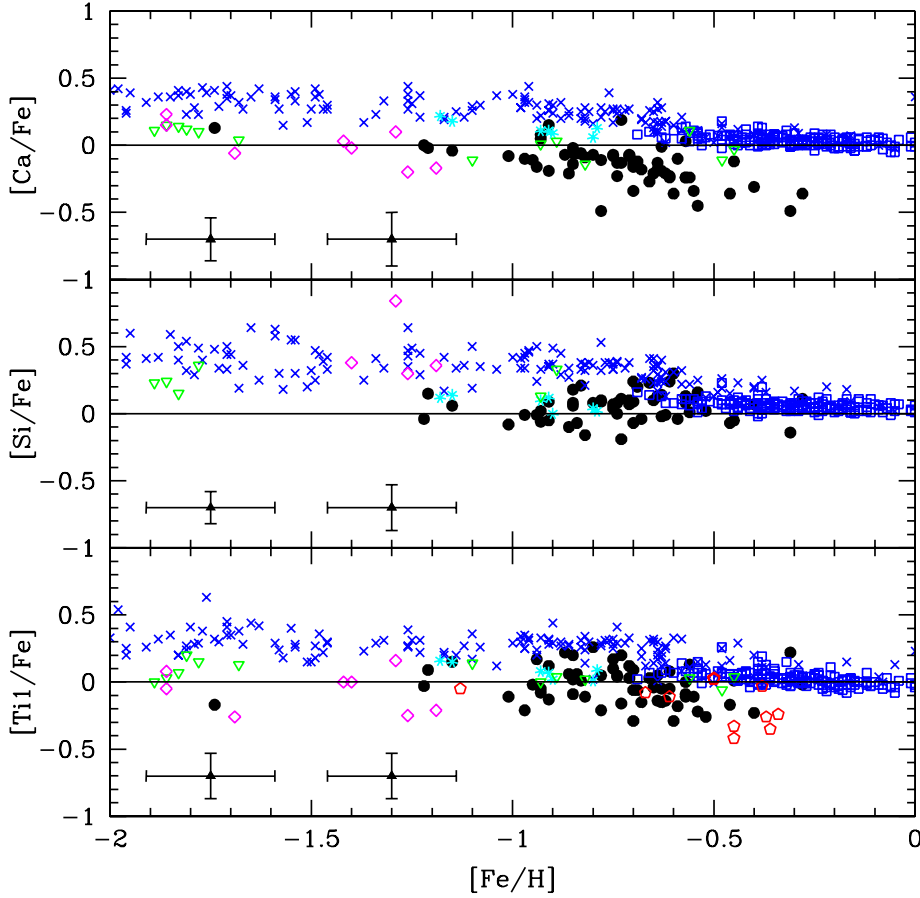


**Fig. 8.** Abundance distributions for the Inner Disk LMC stars:  $[\alpha/\text{Fe}]$  vs.  $[\text{Fe}/\text{H}]$  (blue dots). LMC samples are depicted with polygons (downward-pointing green triangles - Hill et al. 2000; red pentagons - Smith et al. 2002; magenta diamonds - Johnson et al. 2006); and the remaining symbols (all in blue) are data for the galactic stars (crosses - Fulbright 2000; open squares - Reddy et al. 2003; cyan asterisks - Nissen & Schuster 1997). Error bars depict: a. leftmost side of the plots - errors due to stellar parameter uncertainties (Table 8); and b. more to the right side - errors associated with the abundance analysis - for those derived from the EW, is the mean error of Tables 4,5, and 6; for those elements with abundances derived from spectrum synthesis, is the value described in Sect. 4.

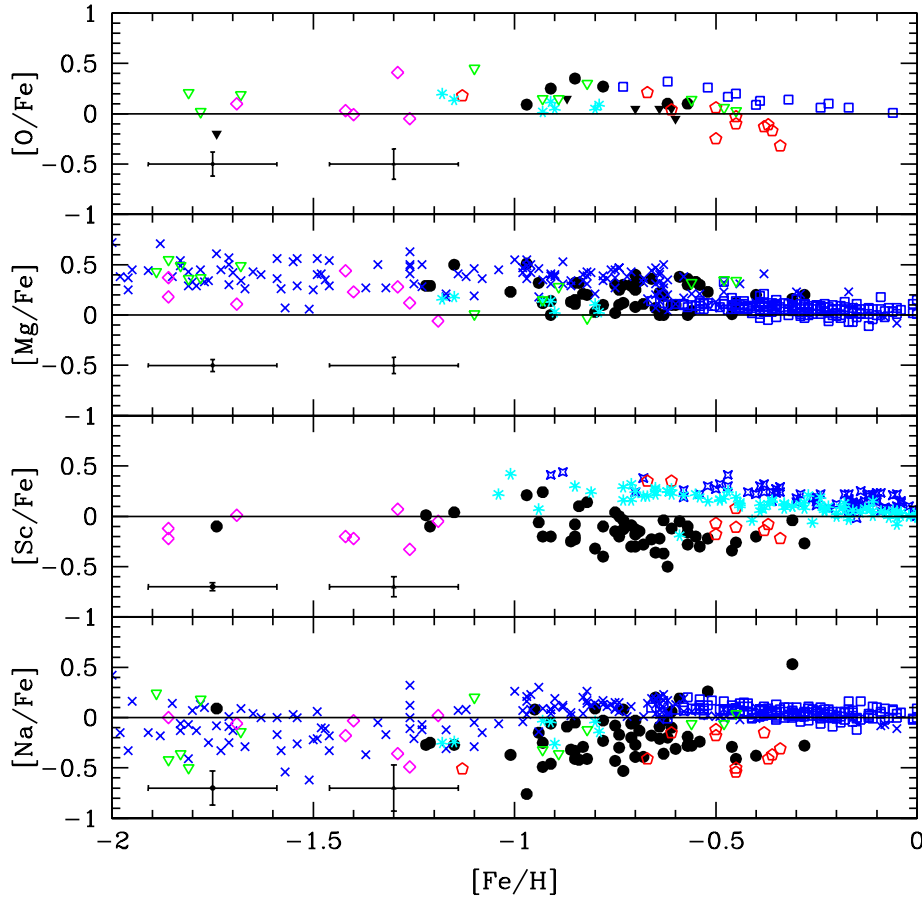


**Fig. 9.** Abundance distributions for the Inner Disk LMC stars:  $[O, Mg, Na, Sc/Fe]$  vs.  $[Fe/H]$  (symbols are the same as in Fig. 8, and we added: blue open stars - Allende Prieto et al. 2004, blue crosses - Bensby et al. 2004 only for oxygen; cyan asterisks - Nissen et al. 2000 for Sc and Nissen & Schuster 1997 for the other elements).

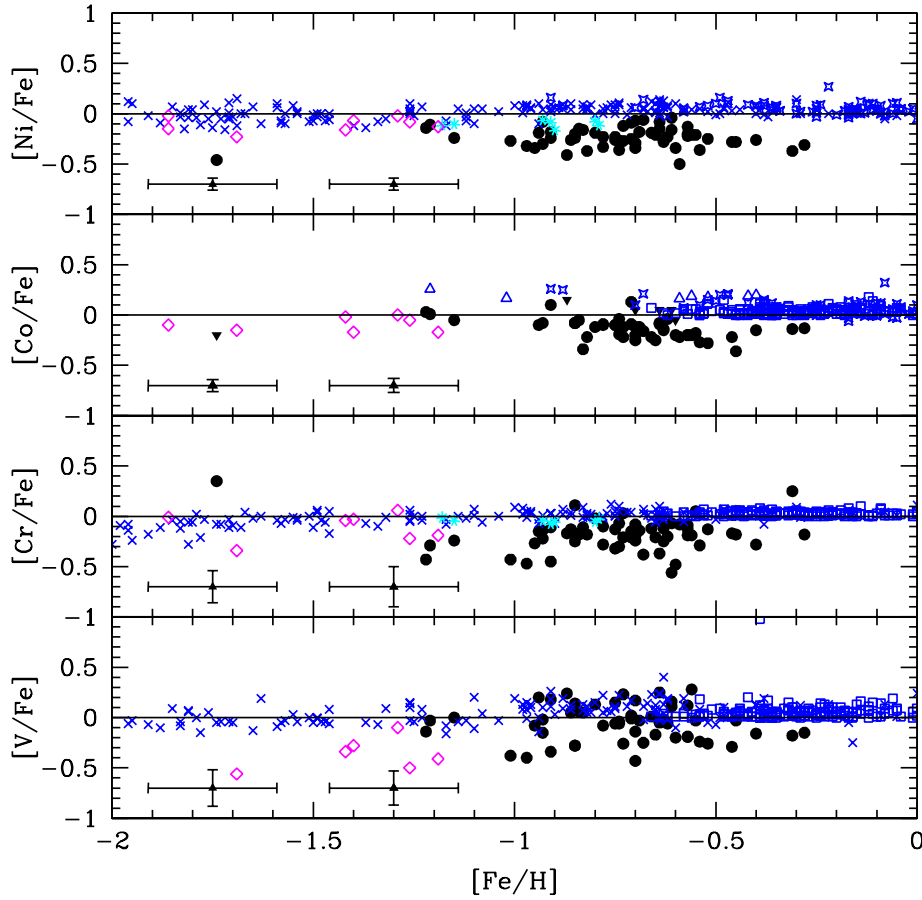


**Fig. 10.** Abundance distributions for the Inner Disk LMC stars: [Iron-peak/Fe] vs. [Fe/H] (symbols are the same as in Figs. 8 and 9, and the solid downtriangles depict upper limits for our sample stars).

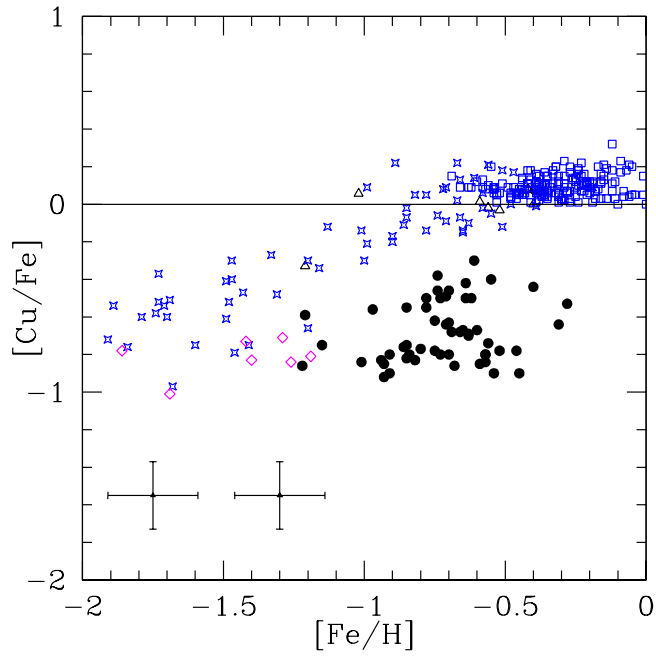


**Fig. 11.** Abundance distributions for Inner Disk LMC stars: Copper. The symbols are the data from: our sample stars (dots); Mishenina et al. 2002 (blue stars); Prochaska et al. 2002 (open blue triangles); Reddy et al. 2003 (open blue squares); Johnson et al. 2006 (magenta diamonds).



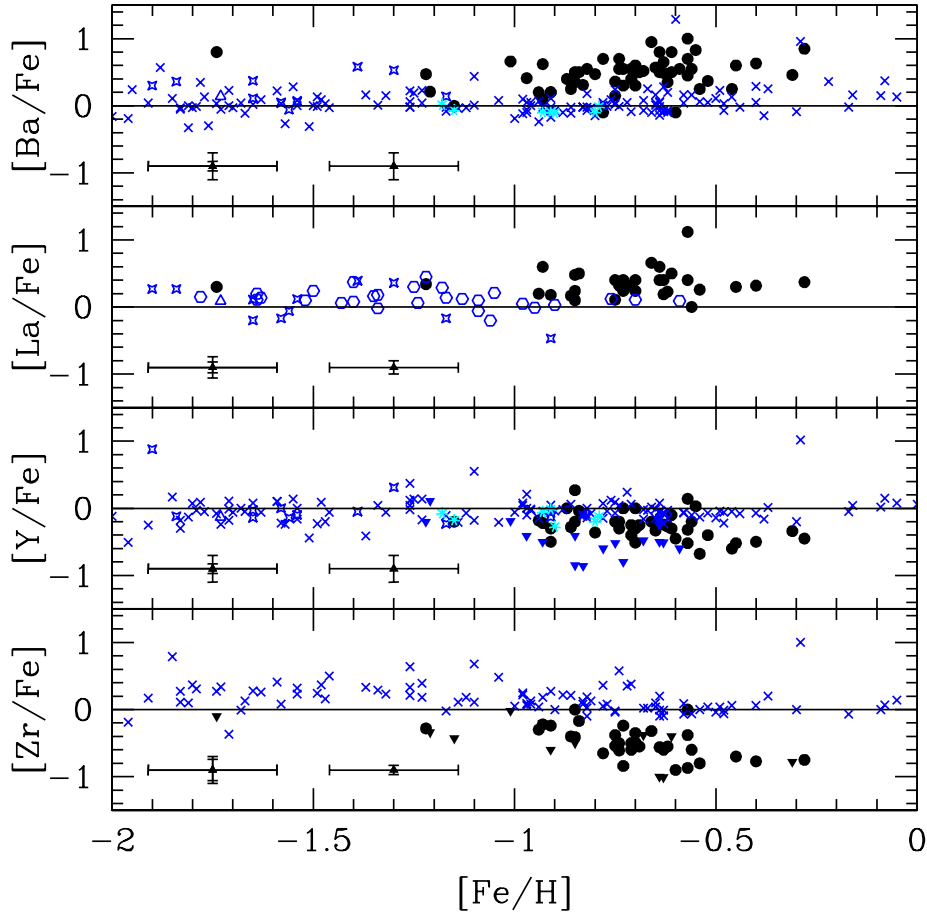


**Fig. 12.** Abundance distributions for Inner Disk LMC stars: [*s*-elements/Fe] vs. [Fe/H]. The large dots (or downtriangles for upper limits) depict our sample stars, while open blue symbols represent galactic samples: symbols as in Figure 8, plus Burris et al. 2000 (blue stars); Johnson & Bolte 2002 (blue triangles); Simmerer et al. 2004 (blue hexagons); Nissen & Schuster 1997 (cyan asterisks).

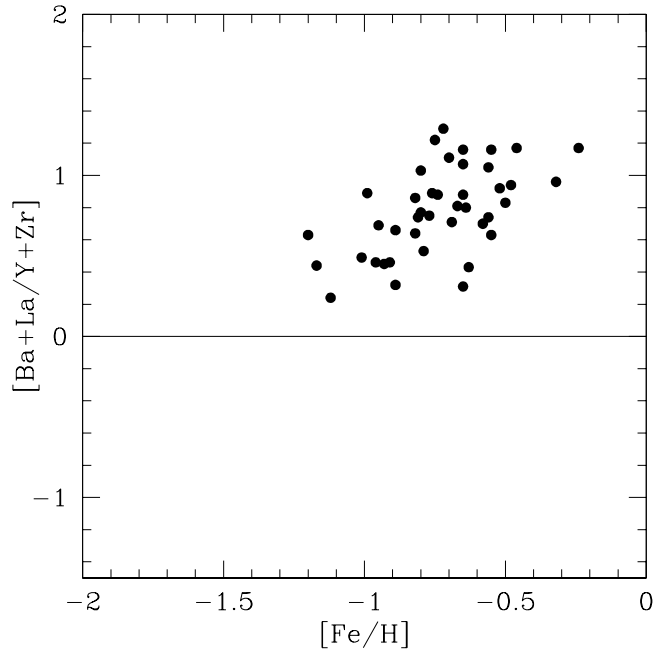


**Fig. 13.** Observed abundance ratios  $[hs/ls] = [Ba+La/Y+Zr]$ .

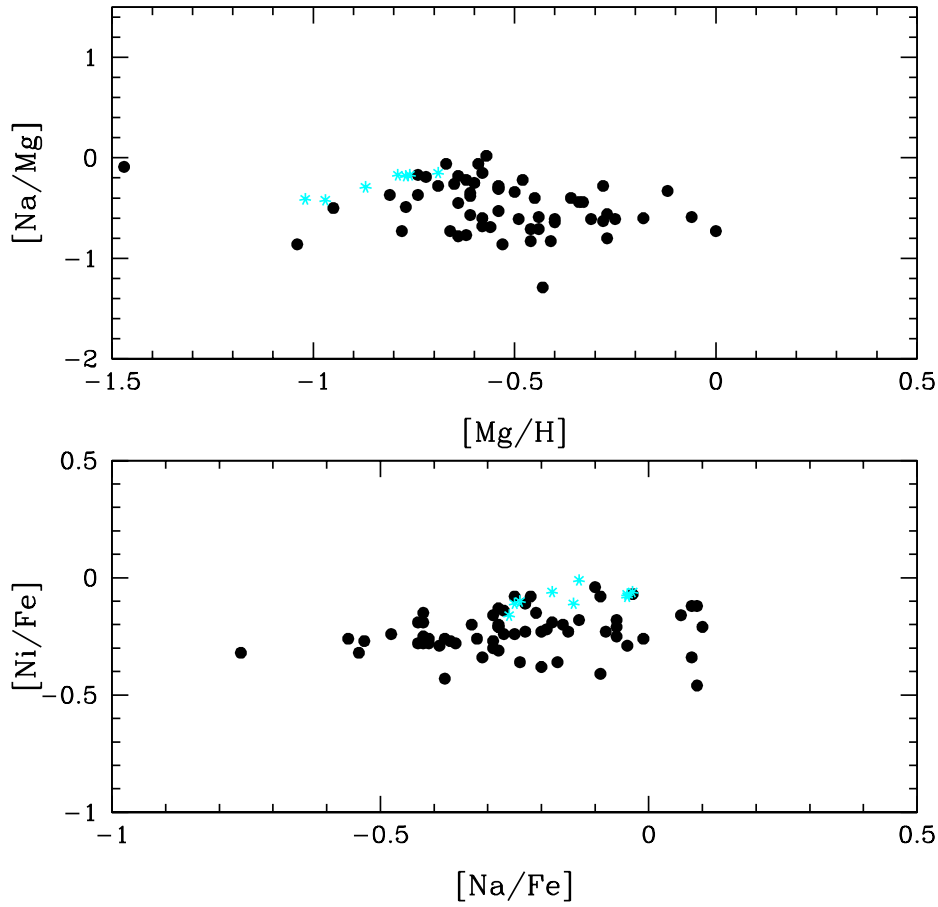


**Fig. 14.** The NaNi and NaMg abundance relations. Our sample stars are depicted as dots and NS97 low- $\alpha$  stars as starred symbols.

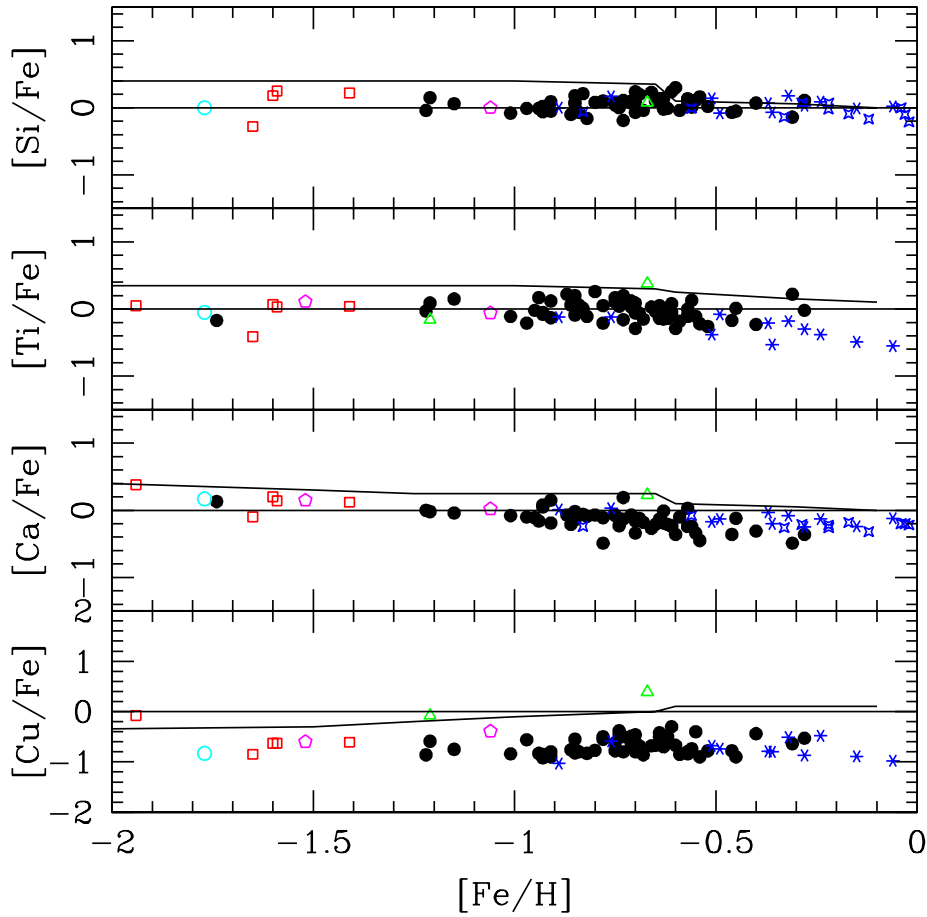


**Fig. 15.** Comparison of the Inner Disk LMC stars with stars from the dwarf spheroidal galaxies and the Sgr galaxy. 1. Alpha elements. The symbols are: our sample (dots), Leo I (magenta pentagons), Sculptor (open cyan dots), Fornax (green triangles), Carina (red squares), and Sgr (Bonifacio et al. 2005 - blue stars; Sbordone et al. 2007 - blue asteriks). Solid lines depict mean values of the Galactic distributions for each element.

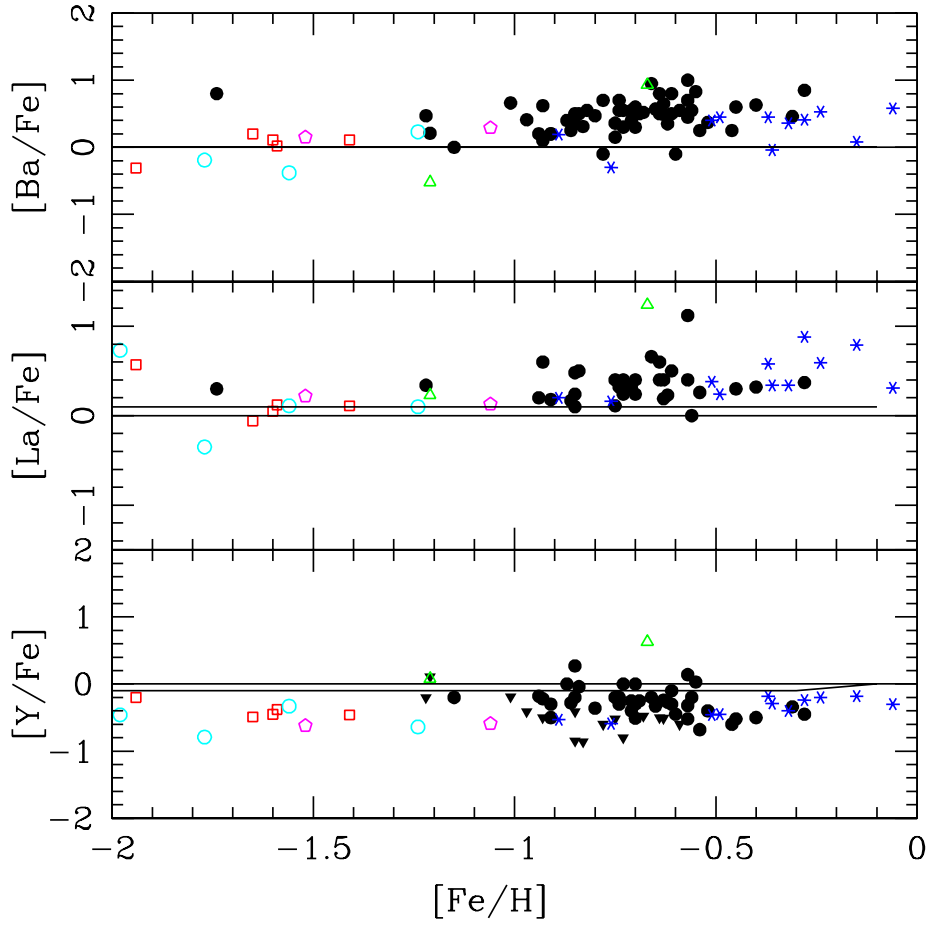


**Fig. 16.** Comparison of the Inner Disk LMC stars with stars from the dwarf spheroidal galaxies. 2. *s*-process elements (symbols are the same as in Fig. 15).

**Table 1.** Photometric Data

Star Reference	2MASS number	V	I	J	K
		mag	mag	mag	mag
RGB_1055	05113508-7112309	17.599	16.219	15.070	14.172
RGB_1105	05125047-7107463	17.661	16.170	14.972	13.952
RGB_1118	05104862-7109301	17.628	16.278	15.298	14.258
RGB_499	05130497-7115406	17.023	15.699	14.624	13.905
RGB_512	05105703-7111340	16.994	15.539	14.452	13.489
RGB_522	05112258-7107277	17.005	15.537	14.360	13.420
RGB_533	05131266-7118005	16.958	15.537	14.562	13.571
RGB_534	05123774-7118119	17.111	15.890	14.807	14.045
RGB_546	05112068-7108113	17.041	15.619	14.546	13.639
RGB_548	05130454-7113055	17.095	15.680	14.502	13.573
RGB_565	05111922-7112564	17.061	15.585	14.468	13.489
RGB_576	05120852-7116597	17.132	15.806	14.668	13.631
RGB_593	05132454-7109519	17.168	15.688	14.484	13.529
RGB_599	05124460-7109195	17.174	15.756	14.574	13.663
RGB_601	05111325-7120037	17.112	15.673	14.633	13.772
RGB_606	05133509-7109322	17.152	15.791	14.694	13.850
RGB_611	05114888-7111492	17.122	15.603	14.478	13.589
RGB_614	05145465-7113031	17.023	15.492	14.459	13.375
RGB_620	05142327-7107446	17.205	15.790	14.608	13.845
RGB_625	05103395-7112074	17.144	15.614	14.473	13.440
RGB_629	05104928-7110057	17.140	15.766	14.723	13.792
RGB_631	05134131-7118477	17.054	15.655	14.638	13.638
RGB_633	05120481-7113402	17.131	15.647	14.527	13.702
RGB_640	05100529-7112259	17.154	15.772	14.747	13.791
RGB_646	05140805-7117297	17.071	15.674	14.653	13.922
RGB_651	05114466-7107176	17.152	15.713	14.672	13.729
RGB_655	05143617-7109412	17.202	15.674	14.521	13.616
RGB_656	05122551-7112106	17.191	15.758	14.637	13.743
RGB_658	05100845-7109582	17.229	15.797	14.728	13.643
RGB_664	05100659-7115514	17.156	15.529	14.438	13.336
RGB_666	05104728-7119320	17.167	15.833	14.763	13.977
RGB_671	05114880-7113428	17.197	15.705	14.555	13.585
RGB_672	05130066-7116289	17.193	15.611	14.460	13.407
RGB_679	05123409-7113324	17.203	15.653	14.481	13.578

**Table 1.** Photometric Data

Star Reference	2MASS number	V	I	J	K
		mag	mag	mag	mag
RGB_690	05144229-7110108	17.266	15.678	14.488	13.413
RGB_699	05095252-7115084	17.214	16.058	15.243	14.399
RGB_700	05113581-7113336	17.284	15.821	14.717	13.676
RGB_701	05124208-7110018	17.214	15.693	14.590	13.579
RGB_705	05141536-7107463	17.215	15.886	14.866	14.026
RGB_710	05110701-7108413	17.308	15.762	14.424	13.368
RGB_720	05103055-7116158	17.314	15.984	14.901	14.313
RGB_728	05142677-7119303	17.249	15.836	14.777	13.955
RGB_731	05120180-7117002	17.255	15.593	14.382	13.357
RGB_748	05122530-7119025	17.279	15.781	14.804	13.760
RGB_752	05144969-7110095	17.320	15.801	14.566	13.621
RGB_756	05143449-7112462	17.251	15.568	14.349	13.278
RGB_758	05111461-7118573	17.269	15.983	14.996	14.266
RGB_766	05111734-7115235	17.343	15.861	14.726	13.779
RGB_773	05115657-7108489	17.264	15.707	14.632	13.602
RGB_775	05095756-7116288	17.261	15.927	14.879	14.100
RGB_776	05111615-7116401	17.287	15.877	14.826	14.033
RGB_782	05104950-7107338	17.291	15.844	14.758	13.761
RGB_789	05121657-7108570	17.310	15.629	14.382	13.267
RGB_793	05110667-7111205	17.319	15.843	14.751	13.783
RGB_834	05112287-7116589	17.355	15.828	-	-
RGB_854	05102155-7118506	17.415	15.997	14.922	14.064
RGB_855	05124558-7116301	17.393	16.001	14.901	13.981
RGB_859	05112287-7116589	17.397	15.883	14.730	13.806
RGB_900	05130400-7113289	17.400	15.983	14.915	14.032

**Table 2.** Stellar Parameters

Star	$T_{\text{photLow}}$	$T_{\text{phot}}$	$T_{\text{spec}}$	$\log g_{\text{phot}}$	$\log g_{\text{spec}}$	$[\text{Fe}/\text{H}]_{\text{spec}}$	$[\text{Fe}/\text{H}]_{\text{CaT}}$	$[\text{FeII}/\text{H}]$	Vt	Rv
RGB_1055	4066	4118	4266	1.5	0.90	-0.96	-0.87	-0.87	1.2	177
RGB_1105	3921	3965	4100	1.4	0.90	-0.71	-1.15	-0.69	1.6	243
RGB_1118	4102	4154	4204	1.5	1.30	-0.57	-0.25	-0.65	1.8	208
RGB_499	4212	4269	4242	1.4	1.00	-0.85	-0.44	-0.89	2.2	220
RGB_512	4002	4051	4202	1.2	0.80	-0.84	-0.78	-0.89	1.7	247
RGB_522	3971	4016	4101	1.2	1.01	-0.70	-0.37	-0.77	2.0	270
RGB_533	4062	4113	4112	1.2	0.80	-0.75	-0.43	-0.82	2.0	243
RGB_534	4295	4359	4295	1.5	1.20	-1.22	-1.11	-1.12	1.6	246
RGB_546	4055	4107	4185	1.3	0.80	-0.96	-0.91	-0.99	1.7	260
RGB_548	4016	4064	4066	1.2	0.90	-0.74	-0.31	-0.80	2.0	247
RGB_565	3970	4016	4100	1.2	0.70	-0.94	-0.60	-0.96	1.9	242
RGB_576	4064	4117	4190	1.3	0.80	-1.24	-1.03	-1.20	1.6	305
RGB_593	3948	3993	4088	1.2	0.70	-1.15	-0.58	-1.17	1.9	234
RGB_599	4018	4066	4028	1.3	0.80	-0.84	-0.71	-0.81	1.8	241
RGB_601	4071	4123	4101	1.3	1.01	-0.55	-0.77	-0.44	2.0	242
RGB_606	4122	4174	4320	1.4	0.80	-1.74	-1.63	-1.72	1.0	183
RGB_611	3968	4010	3980	1.2	0.70	-0.45	-0.42	-0.55	1.6	244
RGB_614	3756	3967	4107	1.1	0.70	-0.87	-0.71	-0.84	2.2	241
RGB_620	4075	4127	4197	1.4	1.30	-0.61	-0.28	-0.74	2.0	197
RGB_625	3910	3951	4090	1.2	0.70	-0.91	-0.86	-0.91	2.2	242
RGB_629	4099	4150	4229	1.3	0.80	-0.91	-0.97	-0.95	1.7	188
RGB_631	4061	4112	4061	1.3	0.80	-0.64	-0.90	-0.75	1.7	256
RGB_633	4015	4067	4015	1.3	0.90	-0.62	-1.21	-0.55	1.9	194
RGB_640	4089	4141	4280	1.3	0.80	-0.93	-0.82	-0.93	1.9	219
RGB_646	4166	4218	4216	1.4	1.20	-0.72	-0.69	-0.63	1.9	236
RGB_651	4039	4091	4089	1.3	1.10	-0.40	-0.51	-0.46	1.8	247
RGB_655	3948	3988	4048	1.2	0.80	-0.57	-0.66	-0.50	1.8	226
RGB_656	4032	4084	4082	1.3	0.80	-0.71	-0.56	-0.65	2.0	233
RGB_658	3987	4033	4087	1.3	1.10	-0.61	-0.40	-0.57	2.0	231
RGB_664	3840	3881	3900	1.1	0.70	-0.54	-0.58	-0.48	1.9	251
RGB_666	4179	4233	4279	1.4	1.00	-1.02	-1.02	-1.01	1.7	225
RGB_671	3952	3996	4052	1.2	0.90	-0.78	-0.55	-0.70	1.9	249
RGB_672	3866	3906	3956	1.2	0.70	-0.68	-0.38	-0.66	1.9	251
RGB_679	3928	3968	3998	1.2	0.80	-0.63	-0.34	-0.67	2.0	253
RGB_690	3843	3883	3950	1.2	0.90	-0.66	-0.23	-0.70	2.0	296



Table 2. continued

Star	$T_{\text{photLow}}$	$T_{\text{phot}}$	$T_{\text{spec}}$	$\log g_{\text{phot}}$	$\log g_{\text{spec}}$	$[\text{FeI}/\text{H}]_{\text{spec}}$	$[\text{FeI}/\text{H}]_{\text{CaT}}$	$[\text{FeII}/\text{H}]$	Vt	Rv
RGB_699	4458	4531	4488	1.6	1.20	-0.64	-1.15	-0.70	1.4	230
RGB_700	3966	4011	4000	1.3	1.01	-0.60	-0.37	-0.56	2.0	282
RGB_701	3934	3975	4125	1.2	0.70	-0.73	-0.33	-0.65	2.1	257
RGB_705	4182	4237	4202	1.4	1.20	-0.55	-0.72	-0.50	1.6	250
RGB_710	3834	3870	3950	1.1	0.80	-0.75	-0.65	-0.53	1.9	265
RGB_720	3814	4320	4370	1.6	1.40	-0.82	-0.90	-0.85	1.7	200
RGB_728	4102	4153	4252	1.4	0.90	-0.85	-0.80	-0.76	2.1	270
RGB_731	3804	3844	3900	1.1	0.80	-0.48	-0.23	-0.38	1.8	278
RGB_748	3980	4026	4186	1.3	0.90	-0.35	-0.17	-0.32	1.5	223
RGB_752	3915	3956	3915	1.2	1.01	-0.28	-0.08	-0.24	1.8	225
RGB_756	3780	3813	3930	1.1	0.70	-0.82	-0.46	-0.75	2.0	254
RGB_758	4282	4347	4442	1.6	1.20	-0.95	-1.22	-0.92	1.7	257
RGB_766	3971	4016	4156	1.3	0.90	-0.64	-0.46	-0.65	1.9	282
RGB_773	3914	3954	4034	1.2	0.80	-0.87	-0.51	-0.76	2.4	232
RGB_775	4191	4245	4271	1.5	1.01	-0.82	-1.28	-0.82	1.2	241
RGB_776	4118	4170	4178	1.4	1.01	-0.73	-0.75	-0.72	1.7	241
RGB_782	3998	4045	4078	1.3	0.90	-0.57	-0.34	-0.52	1.8	249
RGB_789	3763	3796	3923	1.1	0.60	-0.56	-0.36	-0.58	1.8	245
RGB_793	3982	4029	4169	1.3	0.80	-0.70	-0.53	-0.80	1.9	241
RGB_834	3953	3993	4053	1.3	0.80	-0.86	-0.64	-0.79	2.0	197
RGB_854	4077	4129	4157	1.4	1.20	-0.70	-0.10	-0.82	2.0	313
RGB_855	4065	4117	4257	1.4	1.20	-0.74	-0.02	-0.73	1.9	217
RGB_859	3951	3992	4021	1.3	1.01	-0.64	-0.22	-0.56	1.9	244
RGB_900	4071	4123	4131	1.4	1.01	-0.69	-0.27	-0.64	2.1	276

**Table 3.** Line List

Wavelength	Element	$\chi_{exc}$	log gf	Wavelength	Element	$\chi_{exc}$	log gf
6496.900	BA2	0.604	-0.380	6393.610	FE1	2.430	-1.580
6572.800	CA1	0.000	-4.300	6344.160	FE1	2.430	-2.920
6162.190	CA1	1.900	-0.090	6593.870	FE1	2.437	-2.420
6169.560	CA1	2.520	-0.270	5701.560	FE1	2.560	-2.220
6169.040	CA1	2.520	-0.540	6609.120	FE1	2.560	-2.690
5601.290	CA1	2.520	-0.690	6475.630	FE1	2.560	-2.940
6493.790	CA1	2.521	0.140	6137.700	FE1	2.590	-1.400
6166.440	CA1	2.521	-0.900	6322.690	FE1	2.590	-2.430
6499.650	CA1	2.523	-0.590	6575.040	FE1	2.590	-2.710
6161.300	CA1	2.523	-1.030	6200.320	FE1	2.610	-2.440
6455.610	CA1	2.523	-1.360	6180.210	FE1	2.730	-2.650
6439.080	CA1	2.526	0.470	6518.370	FE1	2.830	-2.300
6471.670	CA1	2.526	-0.590	6355.040	FE1	2.840	-2.290
6508.840	CA1	2.526	-2.110	6411.660	FE1	3.650	-0.720
5647.240	CO1	2.280	-1.560	6301.510	FE1	3.650	-0.600
6330.100	CR1	0.940	-2.910	6302.500	FE1	3.690	-0.910
6362.880	CR1	0.940	-2.700	6336.830	FE1	3.690	-1.050
5787.930	CR1	3.320	-0.080	6408.030	FE1	3.690	-1.000
5783.070	CR1	3.320	-0.500	5809.220	FE1	3.883	-1.690
5782.130	CU1	1.642	-1.720	6188.020	FE1	3.940	-1.720
6358.690	FE1	0.860	-4.470	6157.730	FE1	4.076	-1.110
6498.950	FE1	0.960	-4.700	6165.360	FE1	4.142	-1.470
6574.250	FE1	0.990	-5.020	6380.750	FE1	4.190	-1.380
6581.220	FE1	1.480	-4.860	5618.630	FE1	4.209	-1.260
6430.860	FE1	2.180	-2.010	5638.270	FE1	4.220	-0.870
6151.620	FE1	2.180	-3.300	5635.820	FE1	4.256	-1.740
6335.340	FE1	2.200	-2.180	5641.450	FE1	4.260	-1.180
6297.800	FE1	2.220	-2.740	5814.810	FE1	4.283	-1.820
6173.340	FE1	2.220	-2.880	5717.830	FE1	4.284	-0.980
6421.350	FE1	2.279	-2.010	5705.470	FE1	4.301	-1.360
6481.880	FE1	2.280	-2.980	5691.500	FE1	4.301	-1.370
6392.540	FE1	2.280	-4.030	5619.610	FE1	4.390	-1.700
6608.040	FE1	2.280	-4.030	5806.730	FE1	4.607	-0.900
6494.990	FE1	2.400	-1.270	5679.020	FE1	4.651	-0.770

Table 3. continued.

Wavelength	Element	$\chi_{exc}$	log gf	Wavelength	Element	$\chi_{exc}$	log gf
6597.560	FE1	4.795	-0.920	5793.070	SI1	4.930	-2.060
6469.190	FE1	4.835	-0.620	6599.110	TI1	0.900	-2.085
5633.950	FE1	4.990	-0.270	6126.220	TI1	1.070	-1.420
6516.080	FE2	2.890	-3.450	6261.110	TI1	1.430	-0.480
61432.68	FE2	2.890	-3.708	6554.240	TI1	1.440	-1.220
6149.250	FE2	3.889	-2.724	6303.770	TI1	1.440	-1.570
6247.560	FE2	3.890	-2.329	6258.100	TI1	1.443	-0.350
6416.920	FE2	3.891	-2.740	6556.080	TI1	1.460	-1.080
6456.390	FE2	3.900	-2.075	5648.580	TI1	2.490	-0.250
6320.430	LA2	0.170	-1.520	6559.590	TI2	2.048	-2.190
5711.090	MG1	4.346	-1.833	6491.560	TI2	2.061	-1.793
5688.220	NA1	2.100	-0.460	6606.950	TI2	2.061	-2.790
5682.650	NA1	2.100	-0.700	6274.660	V1	0.270	-1.670
6160.750	NA1	2.100	-1.230	6285.170	V1	0.280	-1.510
6154.230	NA1	2.100	-1.530	6199.190	V1	0.290	-1.290
6327.600	NI1	1.680	-3.150	6292.820	V1	0.290	-1.470
6128.980	NI1	1.680	-3.330	6224.510	V1	0.290	-2.010
6314.670	NI1	1.930	-1.770	6251.820	V1	0.290	-1.300
6482.810	NI1	1.930	-2.630	6150.150	V1	0.300	-1.790
6532.890	NI1	1.935	-3.390	6135.370	V1	1.050	-0.750
6586.320	NI1	1.950	-2.810	6119.530	V1	1.060	-0.320
6175.370	NI1	4.090	-0.530	6452.320	V1	1.190	-1.210
6300.310	O1	0.000	-9.770	6531.410	V1	1.218	-0.840
5657.150	SC2	1.500	-0.603	6357.290	V1	1.849	-0.910
5665.560	SI1	4.920	-1.720	6435.010	Y1	0.070	-0.820
5690.430	SI1	4.930	-1.870	6134.570	ZR1	0.000	-1.280

**Table 4.** Abundance ratios of the elements. Iron and Si, Ca, Ti1 and Ti2.

Star	[Fe/H]	[Si/Fe]	[Ca/Fe]	[Ti1/Fe]	[Ti2/Fe]
RGB_1055	-0.96 ± 0.16	-0.01 ± 0.09	-0.10 ± 0.05	-0.21 ± 0.04	-0.06 ± 0.12
RGB_1105	-0.73 ± 0.16	0.04 ± 0.21	-0.07 ± 0.11	0.10 ± 0.12	0.01 ± 0.09
RGB_1118	-0.57 ± 0.16	0.13 ± 0.07	0.03 ± 0.12	0.00 ± 0.06	0.13 ± 0.03
RGB_499	-0.85 ± 0.16	0.18 ± 0.05	-0.06 ± 0.09	0.20 ± 0.05	-0.06 ± 0.13
RGB_512	-0.84 ± 0.16	-0.07 ± 0.08	-0.06 ± 0.08	0.06 ± 0.04	-0.04 ± 0.03
RGB_522	-0.70 ± 0.16	0.24 ± 0.04	-0.13 ± 0.07	0.09 ± 0.02	0.22 ± 0.03
RGB_533	-0.75 ± 0.16	0.07 ± 0.04	-0.08 ± 0.10	0.17 ± 0.04	-0.06 ± 0.12
RGB_534	-1.21 ± 0.16	0.15 ± 0.13	-0.02 ± 0.05	0.09 ± 0.05	0.17 ± 0.14
RGB_546	-0.93 ± 0.16	-0.06 ± 0.16	0.05 ± 0.09	-0.08 ± 0.04	-0.07 ± 0.04
RGB_548	-0.74 ± 0.16	0.08 ± 0.08	-0.23 ± 0.09	0.04 ± 0.04	-0.09 ± 0.09
RGB_565	-0.95 ± 0.16	-0.01 ± 0.03	-0.16 ± 0.03	0.17 ± 0.03	0.00 ± 0.06
RGB_576	-1.24 ± 0.16	-0.04 ± 0.12	0.00 ± 0.04	-0.03 ± 0.03	0.05 ± 0.04
RGB_593	-1.15 ± 0.16	0.06 ± 0.13	-0.04 ± 0.10	0.15 ± 0.05	0.00 ± 0.27
RGB_599	-0.85 ± 0.16	0.06 ± 0.05	-0.14 ± 0.08	-0.09 ± 0.02	0.05 ± 0.14
RGB_601	-0.52 ± 0.17	0.11 ± 0.09	-0.34 ± 0.11	-0.11 ± 0.05	-0.09 ± 0.05
RGB_606	-1.74 ± 0.16	- ± -	0.13 ± 0.08	-0.17 ± 0.08	0.21 ± 0.25
RGB_611	-0.45 ± 0.16	-0.05 ± 0.04	-0.12 ± 0.14	0.01 ± 0.08	-0.14 ± 0.05
RGB_614	-0.87 ± 0.17	- ± -	-0.07 ± 0.08	0.22 ± 0.04	-0.01 ± 0.11
RGB_620	-0.61 ± 0.17	0.24 ± 0.10	-0.23 ± 0.08	0.08 ± 0.09	0.28 ± 0.08
RGB_625	-0.91 ± 0.16	0.09 ± 0.05	0.15 ± 0.08	0.12 ± 0.04	0.09 ± 0.10
RGB_629	-0.91 ± 0.16	-0.05 ± 0.09	-0.19 ± 0.06	-0.13 ± 0.03	0.05 ± 0.06
RGB_631	-0.63 ± 0.16	-0.02 ± 0.12	-0.01 ± 0.12	-0.05 ± 0.06	0.04 ± 0.03
RGB_633	-0.62 ± 0.16	-0.01 ± 0.14	-0.21 ± 0.07	-0.14 ± 0.06	0.06 ± 0.16
RGB_640	-0.93 ± 0.16	0.02 ± 0.11	0.08 ± 0.09	-0.05 ± 0.05	0.07 ± 0.08
RGB_646	-0.69 ± 0.16	-0.04 ± 0.05	-0.18 ± 0.15	-0.15 ± 0.07	-0.01 ± 0.08
RGB_651	-0.40 ± 0.16	0.07 ± 0.08	-0.31 ± 0.10	-0.23 ± 0.04	-0.11 ± 0.05
RGB_655	-0.57 ± 0.16	0.13 ± 0.03	-0.24 ± 0.08	-0.09 ± 0.05	-0.02 ± 0.09
RGB_656	-0.71 ± 0.16	0.07 ± 0.06	-0.07 ± 0.09	0.03 ± 0.11	0.02 ± 0.23
RGB_658	-0.61 ± 0.16	- ± -	-0.24 ± 0.07	-0.05 ± 0.05	-0.06 ± 0.26
RGB_664	-0.54 ± 0.16	0.16 ± 0.08	-0.45 ± 0.07	-0.22 ± 0.07	0.00 ± 0.18
RGB_666	-1.02 ± 0.16	-0.08 ± 0.13	-0.08 ± 0.08	-0.11 ± 0.09	-0.06 ± 0.06
RGB_671	-0.78 ± 0.16	0.10 ± 0.08	-0.11 ± 0.11	-0.21 ± 0.02	-0.06 ± 0.03
RGB_672	-0.65 ± 0.17	0.10 ± 0.05	-0.21 ± 0.22	-0.04 ± 0.07	0.09 ± 0.13
RGB_679	-0.63 ± 0.16	0.14 ± 0.04	-0.19 ± 0.09	-0.15 ± 0.07	-0.08 ± 0.05

Table 4. continued.

Star	[Fe/H]	[Si/Fe]	[Ca/Fe]	[Ti1/Fe]	[Ti2/Fe]
RGB_690	$-0.66 \pm 0.16$	$0.23 \pm 0.04$	$-0.27 \pm 0.09$	$0.03 \pm 0.03$	$-0.10 \pm 0.05$
RGB_699	$-0.59 \pm 0.16$	$-0.04 \pm 0.17$	$-0.10 \pm 0.09$	$-0.18 \pm 0.04$	$-0.09 \pm 0.24$
RGB_700	$-0.60 \pm 0.16$	$0.30 \pm 0.14$	$-0.36 \pm 0.10$	$-0.29 \pm 0.03$	$-0.10 \pm 0.12$
RGB_701	$-0.73 \pm 0.17$	$0.11 \pm 0.09$	$0.19 \pm 0.13$	$0.20 \pm 0.07$	$0.00 \pm 0.09$
RGB_705	$-0.52 \pm 0.16$	$0.02 \pm 0.06$	$- \pm 0.16$	$-0.26 \pm 0.04$	$-0.06 \pm 0.05$
RGB_710	$-0.70 \pm 0.16$	$0.09 \pm 0.11$	$-0.34 \pm 0.13$	$-0.29 \pm 0.10$	$0.02 \pm 0.06$
RGB_720	$-0.83 \pm 0.16$	$0.21 \pm 0.10$	$-0.06 \pm 0.08$	$0.01 \pm 0.04$	$0.15 \pm 0.12$
RGB_728	$-0.85 \pm 0.16$	$0.08 \pm 0.08$	$-0.02 \pm 0.07$	$0.02 \pm 0.06$	$0.35 \pm 0.13$
RGB_731	$-0.46 \pm 0.17$	$-0.07 \pm 0.09$	$-0.36 \pm 0.13$	$-0.17 \pm 0.12$	$-0.11 \pm 0.16$
RGB_748	$-0.31 \pm 0.17$	$-0.14 \pm 0.10$	$-0.49 \pm 0.08$	$0.22 \pm 0.07$	$- \pm 0.09$
RGB_752	$-0.28 \pm 0.16$	$0.11 \pm 0.04$	$-0.36 \pm 0.09$	$-0.02 \pm 0.07$	$-0.01 \pm 0.08$
RGB_756	$-0.80 \pm 0.17$	$0.08 \pm 0.05$	$-0.07 \pm 0.15$	$0.26 \pm 0.12$	$-0.04 \pm 0.08$
RGB_758	$-0.95 \pm 0.16$	$- \pm -$	$-0.11 \pm 0.08$	$-0.02 \pm 0.10$	$-0.05 \pm 0.14$
RGB_766	$-0.64 \pm 0.17$	$0.13 \pm 0.15$	$-0.18 \pm 0.07$	$0.05 \pm 0.04$	$-0.02 \pm 0.04$
RGB_773	$-0.78 \pm 0.17$	$0.09 \pm 0.09$	$-0.49 \pm 0.13$	$0.05 \pm 0.07$	$0.15 \pm 0.16$
RGB_775	$-0.82 \pm 0.16$	$-0.16 \pm 0.11$	$-0.09 \pm 0.10$	$-0.11 \pm 0.07$	$-0.10 \pm 0.18$
RGB_776	$-0.73 \pm 0.16$	$-0.19 \pm 0.08$	$-0.13 \pm 0.08$	$-0.16 \pm 0.05$	$0.03 \pm 0.03$
RGB_782	$-0.57 \pm 0.16$	$0.08 \pm 0.09$	$-0.24 \pm 0.09$	$-0.11 \pm 0.03$	$-0.07 \pm 0.07$
RGB_789	$-0.56 \pm 0.16$	$0.01 \pm 0.03$	$-0.24 \pm 0.08$	$0.13 \pm 0.07$	$0.04 \pm 0.09$
RGB_793	$-0.70 \pm 0.16$	$-0.07 \pm 0.06$	$-0.16 \pm 0.08$	$-0.06 \pm 0.05$	$0.01 \pm 0.06$
RGB_834	$-0.86 \pm 0.16$	$-0.10 \pm 0.06$	$-0.21 \pm 0.05$	$0.06 \pm 0.07$	$0.11 \pm 0.03$
RGB_854	$-0.70 \pm 0.16$	$0.10 \pm 0.08$	$-0.08 \pm 0.08$	$0.12 \pm 0.14$	$-0.06 \pm 0.33$
RGB_855	$-0.74 \pm 0.16$	$0.00 \pm 0.09$	$-0.13 \pm 0.09$	$0.05 \pm 0.06$	$0.11 \pm 0.18$
RGB_859	$-0.64 \pm 0.16$	$0.13 \pm 0.09$	$-0.13 \pm 0.12$	$-0.14 \pm 0.04$	$0.17 \pm 0.05$
RGB_900	$-0.69 \pm 0.16$	$0.20 \pm 0.05$	$-0.12 \pm 0.09$	$-0.06 \pm 0.03$	$0.09 \pm 0.10$

**Table 5.** Abundance ratios of the elements. Na, Sc, Cu and the  $\alpha$ -elements Mg and O.

Star	[O/Fe]	[Mg/Fe]	[Na/Fe]	[Sc/Fe]	[Cu/Fe]
RGB_1055	0.10	0.50	-0.76 $\pm$ 0.05	0.20	-0.57
RGB_1105	-	0.02	-0.43 $\pm$ 0.07	0.04	-0.78
RGB_1118	0.10	0.00	-0.28 $\pm$ 0.10	-0.16	-0.84
RGB_499	0.40	0.15	-0.05 $\pm$ 0.07	-0.23	-0.55
RGB_512	-	0.32	-0.42 $\pm$ 0.07	0.10	-0.80
RGB_522	-	0.40	-0.03 $\pm$ 0.15	-0.18	-0.46
RGB_533	-	0.30	-0.08 $\pm$ 0.07	-0.15	-0.62
RGB_534	-	0.28	-0.25 $\pm$ 0.05	-0.11	-0.60
RGB_546	-	0.10	-0.49 $\pm$ 0.13	0.22	-0.94
RGB_548	-	0.25	-0.30 $\pm$ 0.10	0.00	-0.46
RGB_565	-	0.32	-0.15 $\pm$ 0.07	-0.06	-0.83
RGB_576	-	0.31	-0.27 $\pm$ 0.05	0.03	-0.84
RGB_593	-	0.50	-0.27 $\pm$ 0.06	0.04	-0.75
RGB_599	-	0.30	-0.41 $\pm$ 0.06	-0.10	-0.84
RGB_601	-	0.33	- $\pm$ 0.07	-0.20	-0.40
RGB_606	<-0.20	-	0.09 $\pm$ 0.08	-0.10	-
RGB_611	-	0.12	-0.41 $\pm$ 0.13	-0.26	-0.90
RGB_614	<0.15	-	-0.09 $\pm$ 0.05	-	-
RGB_620	<0.05	0.10	0.06 $\pm$ 0.17	-0.12	-0.30
RGB_625	-	0.00	-0.06 $\pm$ 0.07	-0.20	-0.80
RGB_629	0.30	0.14	-0.46 $\pm$ 0.10	0.00	-0.90
RGB_631	-	0.20	-0.03 $\pm$ 0.10	-0.03	-0.68
RGB_633	0.10	-	-0.20 $\pm$ 0.07	-0.50	-0.50
RGB_640	-	0.12	-0.25 $\pm$ 0.05	-0.20	-0.85
RGB_646	-	0.17	-0.39 $\pm$ 0.08	-0.22	-0.80
RGB_651	-	0.15	-0.38 $\pm$ 0.14	-0.20	-0.44
RGB_655	-	0.36	-0.28 $\pm$ 0.14	-0.10	-0.80
RGB_656	-	0.30	-0.06 $\pm$ 0.12	-0.30	-0.64
RGB_658	-	-	-0.10 $\pm$ 0.09	-	-
RGB_664	-	0.30	-0.24 $\pm$ 0.12	-0.30	-0.90
RGB_666	-	0.22	-0.37 $\pm$ 0.07	-	-0.85
RGB_671	-	-	-0.23 $\pm$ 0.08	-0.10	-0.50
RGB_672	-	0.10	0.20 $\pm$ 0.14	-0.33	-0.64
RGB_679	-	0.00	-0.36 $\pm$ 0.09	-0.37	-0.70

Table 5. continued.

Star	[O/Fe]	[Mg/Fe]	[Na/Fe]	[Sc/Fe]	[Cu/Fe]
RGB_690	-	0.36	$-0.18 \pm 0.12$	-0.23	-0.68
RGB_699	-	0.42	$0.19 \pm 0.08$	0.00	-0.80
RGB_700	<-0.05	0.10	$-0.31 \pm 0.11$	<-0.20	-0.67
RGB_701	-	0.30	$0.08 \pm 0.10$	-0.04	-0.50
RGB_705	-	0.26	$0.26 \pm 0.09$	-0.19	-0.75
RGB_710	-	0.30	$-0.27 \pm 0.08$	-0.08	-0.58
RGB_720	<0.35	0.20	$-0.29 \pm 0.11$	<-0.30	-
RGB_728	-	0.11	$-0.33 \pm 0.07$	-0.20	-0.75
RGB_731	0.00	0.03	$-0.29 \pm 0.08$	-0.32	-0.76
RGB_748	<0.00	0.20	$0.53 \pm 0.20$	0.00	-0.60
RGB_752	-	0.20	$-0.28 \pm 0.12$	-0.27	-0.53
RGB_756	-	0.05	$0.09 \pm 0.08$	<-0.30	-0.75
RGB_758	-	-	$0.08 \pm 0.12$	-	-
RGB_766	<0.10	0.00	$-0.09 \pm 0.13$	-	-0.50
RGB_773	0.25	0.02	$-0.03 \pm 0.07$	-0.32	-0.57
RGB_775	-	0.20	$-0.41 \pm 0.04$	0.14	-0.83
RGB_776	-	0.12	$-0.53 \pm 0.10$	-0.13	-0.80
RGB_782	-	0.30	$-0.19 \pm 0.13$	-0.28	-0.80
RGB_789	-	0.04	$-0.28 \pm 0.14$	-0.30	-0.74
RGB_793	<0.10	0.08	$-0.39 \pm 0.10$	-0.30	-0.80
RGB_834	-	0.13	$-0.32 \pm 0.04$	-0.25	-0.76
RGB_854	-	0.30	$-0.20 \pm 0.12$	-0.10	-0.50
RGB_855	-	0.10	$-0.17 \pm 0.09$	-0.20	-0.38
RGB_859	-	0.22	$-0.21 \pm 0.10$	-0.22	-0.42
RGB_900	-	0.34	$-0.13 \pm 0.11$	-0.15	-0.68

**Table 6.** Abundance ratios of the elements (continuation). FeII and Iron-peak elements.

Star	[Cr/Fe]	[V/Fe]	[Ni/Fe]	[Co/Fe]
RGB_1055	$-0.47 \pm 0.12$	$-0.40 \pm 0.04$	$-0.32 \pm 0.08$	$<0.00$
RGB_1105	$-0.32 \pm 0.11$	$-0.06 \pm 0.05$	$-0.26 \pm 0.08$	$-0.10$
RGB_1118	$-0.19 \pm 0.09$	$-0.19 \pm 0.08$	$-0.20 \pm 0.06$	$-0.20$
RGB_499	$0.11 \pm 0.12$	$0.14 \pm 0.06$	$-0.23 \pm 0.09$	$-0.08$
RGB_512	$-0.18 \pm 0.11$	$0.06 \pm 0.08$	$-0.15 \pm 0.06$	$-0.05$
RGB_522	$-0.08 \pm 0.11$	$0.17 \pm 0.06$	$-0.07 \pm 0.05$	$-0.12$
RGB_533	$-0.13 \pm 0.10$	$0.15 \pm 0.06$	$-0.23 \pm 0.07$	$-0.10$
RGB_534	$-0.29 \pm 0.08$	$-0.03 \pm 0.05$	$-0.11 \pm 0.05$	$0.00$
RGB_546	$-0.22 \pm 0.13$	$-0.15 \pm 0.05$	$-0.30 \pm 0.06$	$-0.10$
RGB_548	$-0.30 \pm 0.10$	$-0.06 \pm 0.06$	$-0.27 \pm 0.08$	$-0.19$
RGB_565	$-0.15 \pm 0.10$	$0.20 \pm 0.05$	$-0.19 \pm 0.04$	$-0.10$
RGB_576	$-0.43 \pm 0.10$	$-0.14 \pm 0.05$	$-0.14 \pm 0.03$	$0.05$
RGB_593	$-0.24 \pm 0.15$	$0.00 \pm 0.05$	$-0.24 \pm 0.06$	$-0.05$
RGB_599	$-0.25 \pm 0.12$	$-0.28 \pm 0.06$	$-0.24 \pm 0.09$	$-0.10$
RGB_601	$0.05 \pm 0.10$	$-0.03 \pm 0.04$	$-0.21 \pm 0.04$	$-0.18$
RGB_606	$0.35 \pm 0.12$	$- \pm 0.36$	$-0.46 \pm 0.07$	$<0.10$
RGB_611	$-0.18 \pm 0.06$	$-0.03 \pm 0.08$	$-0.28 \pm 0.02$	$-0.36$
RGB_614	$-0.17 \pm 0.07$	$0.24 \pm 0.07$	$-0.41 \pm 0.10$	$-$
RGB_620	$-0.07 \pm 0.18$	$0.11 \pm 0.08$	$-0.16 \pm 0.11$	$<0.00$
RGB_625	$-0.11 \pm 0.12$	$0.18 \pm 0.08$	$-0.18 \pm 0.12$	$0.10$
RGB_629	$-0.45 \pm 0.12$	$-0.34 \pm 0.04$	$-0.24 \pm 0.11$	$<-0.20$
RGB_631	$-0.12 \pm 0.12$	$-0.02 \pm 0.07$	$-0.26 \pm 0.06$	$-0.14$
RGB_633	$-0.20 \pm 0.10$	$-0.06 \pm 0.02$	$-0.23 \pm 0.06$	$-0.04$
RGB_640	$-0.14 \pm 0.14$	$-0.02 \pm 0.06$	$-0.08 \pm 0.05$	$<-0.20$
RGB_646	$-0.38 \pm 0.06$	$-0.25 \pm 0.06$	$-0.06 \pm 0.03$	$-0.10$
RGB_651	$-0.28 \pm 0.12$	$-0.16 \pm 0.06$	$-0.26 \pm 0.07$	$-0.15$
RGB_655	$-0.09 \pm 0.12$	$0.12 \pm 0.06$	$-0.13 \pm 0.08$	$-0.20$
RGB_656	$-0.21 \pm 0.12$	$0.02 \pm 0.05$	$-0.25 \pm 0.10$	$-0.09$
RGB_658	$-0.56 \pm 0.08$	$0.16 \pm 0.07$	$-0.04 \pm 0.09$	$-$
RGB_664	$-0.29 \pm 0.09$	$-0.24 \pm 0.07$	$-0.36 \pm 0.11$	$-0.27$
RGB_666	$-0.43 \pm 0.09$	$-0.38 \pm 0.05$	$-0.27 \pm 0.06$	$-$
RGB_671	$-0.28 \pm 0.12$	$-0.08 \pm 0.06$	$-0.23 \pm 0.07$	$-0.09$
RGB_672	$-0.21 \pm 0.12$	$-0.17 \pm 0.05$	$-0.21 \pm 0.04$	$-0.22$
RGB_679	$-0.25 \pm 0.14$	$-0.02 \pm 0.05$	$-0.28 \pm 0.06$	$-0.14$



Table 6. continued.

Star	[Cr/Fe]	[V/Fe]	[Ni/Fe]	[Co/Fe]
RGB_690	$-0.12 \pm 0.12$	$0.01 \pm 0.09$	$-0.19 \pm 0.05$	-0.22
RGB_699	$-0.08 \pm 0.06$	$- \pm 0.06$	$-0.50 \pm 0.17$	-0.17
RGB_700	$-0.48 \pm 0.12$	$-0.20 \pm 0.08$	$-0.34 \pm 0.09$	-0.20
RGB_701	$0.03 \pm 0.07$	$0.23 \pm 0.08$	$-0.12 \pm 0.14$	-0.12
RGB_705	$-0.13 \pm 0.09$	$-0.26 \pm 0.04$	$-0.25 \pm 0.09$	-0.25
RGB_710	$-0.24 \pm 0.05$	$-0.43 \pm 0.04$	$-0.34 \pm 0.06$	-0.20
RGB_720	$-0.11 \pm 0.06$	$0.05 \pm 0.06$	$-0.16 \pm 0.12$	-0.29
RGB_728	$-0.17 \pm 0.12$	$-0.28 \pm 0.08$	$-0.20 \pm 0.12$	-0.08
RGB_731	$-0.17 \pm 0.10$	$-0.29 \pm 0.04$	$-0.28 \pm 0.02$	-0.20
RGB_748	$0.25 \pm 0.15$	$-0.18 \pm 0.13$	$-0.37 \pm 0.13$	-0.10
RGB_752	$-0.18 \pm 0.07$	$-0.15 \pm 0.07$	$-0.31 \pm 0.09$	-0.13
RGB_756	$-0.02 \pm 0.09$	$0.13 \pm 0.05$	$-0.19 \pm 0.09$	-0.10
RGB_758	$-0.27 \pm 0.09$	$-0.08 \pm 0.09$	$-0.34 \pm 0.11$	-
RGB_766	$-0.05 \pm 0.10$	$0.25 \pm 0.07$	$-0.08 \pm 0.03$	-0.09
RGB_773	$-0.10 \pm 0.07$	$- \pm 0.06$	$-0.33 \pm 0.04$	-0.01
RGB_775	$-0.18 \pm 0.06$	$- \pm 0.03$	$-0.37 \pm 0.03$	-0.22
RGB_776	$-0.21 \pm 0.14$	$-0.26 \pm 0.05$	$-0.27 \pm 0.06$	-0.22
RGB_782	$-0.13 \pm 0.10$	$-0.19 \pm 0.07$	$-0.22 \pm 0.02$	-
RGB_789	$-0.19 \pm 0.07$	$0.28 \pm 0.05$	$-0.21 \pm 0.06$	-0.20
RGB_793	$-0.19 \pm 0.13$	$-0.14 \pm 0.05$	$-0.29 \pm 0.06$	-0.20
RGB_834	$-0.13 \pm 0.11$	$0.05 \pm 0.05$	$-0.26 \pm 0.07$	-
RGB_854	$-0.15 \pm 0.12$	$-0.01 \pm 0.09$	$-0.09 \pm 0.05$	0.12
RGB_855	$-0.07 \pm 0.14$	$-0.04 \pm 0.10$	$-0.36 \pm 0.12$	-0.04
RGB_859	$-0.37 \pm 0.11$	$-0.05 \pm 0.05$	$-0.15 \pm 0.03$	-0.08
RGB_900	$-0.14 \pm 0.10$	$-0.03 \pm 0.06$	$-0.18 \pm 0.05$	-0.12

**Table 7.** Abundance ratios of the elements (continuation). Heavy and light *s*-process elements.

Star	[La/Fe]	[Ba/Fe]	[Y/Fe]	[Zr/Fe]	Star	[La/Fe]	[Ba/Fe]	[Y/Fe]	[Zr/Fe]
RGB_1055	<0.05	0.40	<-0.40	-	RGB_666	<0.10	0.65	<-0.20	<-0.30
RGB_1105	0.15	0.40	<-0.48	-0.50	RGB_671	0.15	0.70	<-0.60	-0.65
RGB_1118	1.12	1.00	0.14	0.00	RGB_672	0.20	0.60	-0.30	-0.62
RGB_499	0.48	0.35	0.27	0.00	RGB_679	0.40	0.65	-0.24	-0.60
RGB_512	0.50	0.50	-0.04	-0.17	RGB_690	0.66	0.95	-0.20	-0.32
RGB_522	0.40	0.60	0.00	-0.35	RGB_699	0.12	0.60	<-0.50	-0.80
RGB_533	0.40	0.15	-0.20	-0.38	RGB_700	<0.30	-0.10	-0.45	-0.90
RGB_534	<0.20	0.20	<0.10	<-0.35	RGB_701	0.24	0.30	0.00	-0.24
RGB_546	0.62	0.65	-0.20	-0.20	RGB_705	0.32	0.40	-0.37	-0.80
RGB_548	0.32	0.70	-0.30	-0.61	RGB_710	0.40	0.60	-0.46	-0.78
RGB_565	0.20	0.20	-0.18	-0.30	RGB_720	-	0.35	-	-0.60
RGB_576	0.32	0.45	<-0.20	-0.28	RGB_728	<0.10	0.50	-0.20	<-0.50
RGB_593	<0.20	0.00	-0.20	<-0.45	RGB_731	0.05	0.25	-0.60	-0.70
RGB_599	0.25	0.50	<-0.40	-0.40	RGB_748	<-0.30	0.4	-0.3	<-0.8
RGB_601	-	0.80	0.00	-0.43	RGB_752	0.37	0.85	-0.45	-0.75
RGB_606	0.30	0.80	-	-	RGB_756	0.20	0.45	-0.33	-0.40
RGB_611	0.30	0.60	-0.52	-0.70	RGB_758	-	-	-	-
RGB_614	-	0.40	0.00	-	RGB_766	0.60	0.50	<-0.25	<-1.00
RGB_620	<0.50	0.50	-0.10	<-0.40	RGB_773	0.25	0.00	-0.10	-0.42
RGB_625	0.18	0.20	-0.30	-0.24	RGB_775	0.30	0.60	<-0.80	-0.40
RGB_629	<0.00	0.20	-0.50	<-0.60	RGB_776	0.40	0.55	<-0.80	-0.84
RGB_631	0.20	0.50	<-0.50	<-1.00	RGB_782	<0.10	0.45	-0.52	-0.87
RGB_633	0.23	0.35	-0.27	-0.55	RGB_789	0.00	0.55	-0.20	-0.60
RGB_640	<0.10	0.10	<-0.50	<-0.20	RGB_793	0.24	0.30	-0.30	-0.49
RGB_646	0.47	0.50	<-0.50	<-0.40	RGB_834	0.17	0.25	-0.28	-0.40
RGB_651	0.32	0.63	-0.50	-0.77	RGB_854	<0.35	0.40	-0.25	-0.50
RGB_655	0.40	0.70	-0.32	-0.38	RGB_855	-	0.55	-0.20	-0.50
RGB_656	0.32	0.55	-0.40	-0.60	RGB_859	0.40	0.80	<-0.50	-0.56
RGB_658	-	0.80	-0.30	-	RGB_900	0.40	0.50	-0.25	-0.55
RGB_664	0.26	0.25	-0.68	-0.80					

**Table 8.** Errors due to stellar parameters uncertainties.

Element	$\Delta T_{\text{eff}}=+100$ K	$\Delta \log g=-0.4$	$\Delta V_t=+0.2$ km/s	$\Delta [\text{Fe}/\text{H}]=-0.15$	$\delta_{\text{tot}}$
[Fe I/H]	-0.01	-0.10	-0.12	-0.03	0.16
[O I/FE]	0.04	-0.06	0.10	-0.02	0.12
[V I/FE]	0.16	0.06	0.00	0.04	0.17
[Y I/FE]	0.19	0.08	0.07	0.04	0.22
[Ca I/FE]	0.11	0.11	-0.01	0.04	0.16
[Cr I/FE]	0.12	0.07	0.00	0.04	0.15
[Fe II/Fe]	-0.18	-0.16	0.08	-0.07	0.26
[Mg I/Fe]	0.01	0.06	0.01	0.01	0.06
[Na I/Fe]	0.11	0.10	0.06	0.05	0.17
[Ni I/Fe]	0.01	-0.03	0.05	-0.01	0.06
[Si I/Fe]	-0.07	-0.01	0.09	-0.01	0.12
[Ti I/Fe]	0.15	0.08	0.01	0.04	0.17
[Ti II/Fe]	-0.05	-0.10	0.04	-0.04	0.12
[Zr I/Fe]	0.19	0.06	0.03	0.03	0.20
[Ba II/Fe]	0.04	-0.04	-0.04	0.00	0.07
[Co I/Fe]	0.03	-0.01	0.05	-0.01	0.06
[Cu I/Fe]	0.07	-0.04	0.06	0.07	0.12
[La II/Fe]	0.04	-0.06	0.05	-0.04	0.10
[Sc II/Fe]	-0.01	-0.04	0.01	-0.01	0.04

### Appendix A: Comparison between equivalent width from DAOSPEC and from Splot-Iraf

In order to evaluate the quality of the DAOSPEC estimates, we have derived by eye inspection the EW of six stars, using the Splot Iraf task. We have chosen stars in a range of S/N ratio typical of our total sample in order to better evaluate the errors: S/N = 54 for RGB\_522, 59 for RGB\_546, 47 for RGB\_664, 42 for RGB\_666, 26 for RGB\_720, and 47 for RGB\_1055. The detailed values are given in Table A.1. We have found two problems relative to the DAOSPEC results from GIRAFFE spectra: a) not all blends have been identified, nevertheless all lines with weak blends (which are most of the lines) have been correctly analysed by the iterative process of the program; b) cosmic rays also have not been identified, and those lines too near CR features must be discarded. Therefore the use of DAOSPEC requires spectra and line lists as clear as possible from blends and spectra as clean from cosmic hits as possible. As can be seen in Table A.1, we have found a very good agreement between the program results and those from the Splot manual measurements. The average difference  $\text{EW}(\text{Dao}) - \text{EW}(\text{Splot})$  is  $0.46 \text{ m}\text{\AA}$  for the six stars, with no strong systematic trend in one direction or the other (the mean difference for each star ranges from  $-3.7$  to  $+5 \text{ m}\text{\AA}$ ). However, the dispersion of the

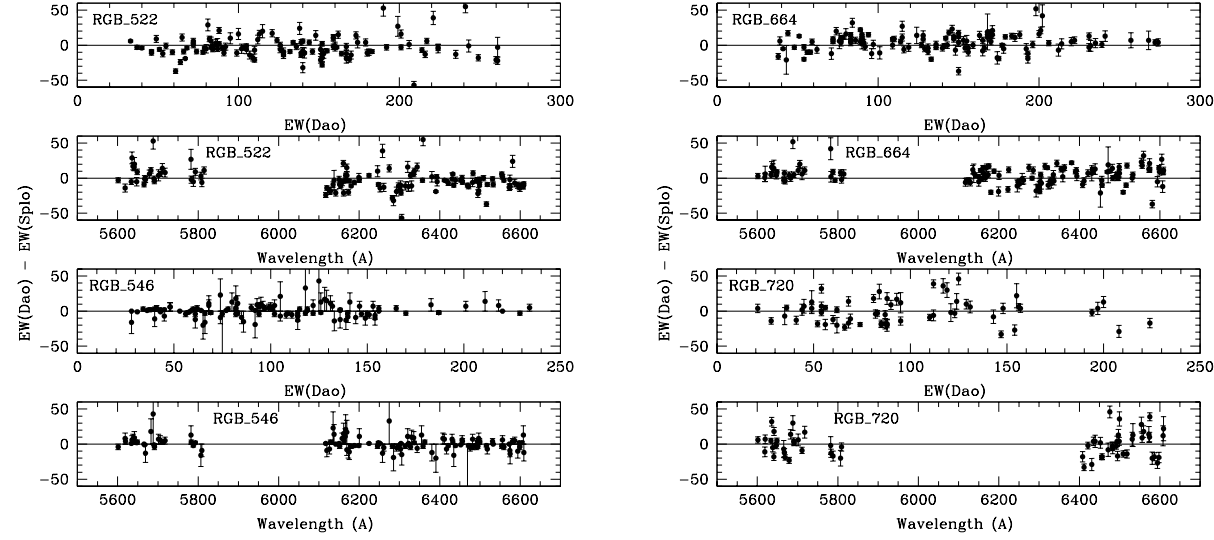


**Fig. A.1.** Difference between the EW derived using the DAOSPEC program and the Iraf task Splot: trends with respect to the EW(Dao) and to the wavelength of the lines for RGB\_522 and RGB\_546 (left plot) and for RGB\_720 and RGB\_664 (right plot).

measurements around the mean are higher, between  $9.4\text{m}\text{\AA}$  for RGB\_1055 and  $22.2\text{m}\text{\AA}$  for RGB\_666. These dispersion seem to anticorrelate with S/N as expected (the two stars with the highest dispersion are the two lowest quality spectra), and may also correlate with temperature, although our sample of 6 stars is not quite high enough to investigate these dependencies any further.

We have checked for systematic trends on the EW with wavelength and with the EW strength by plotting the differences  $\text{EW(Dao)} - \text{EW(Splot)}$  vs. wavelength and  $\text{EW(Dao)} - \text{EW(Splot)}$  vs.  $\text{EW(Dao)}$  for four stars, as shown in Fig. A.1. No trends have been found and confort us in the validity of using DAOSPEC EW mesurement for atmospheric parameter determinations (effective temperature and microturbulence velocities).

In Table A.2 we give the differences for the abundances derived from DAOSPEC and Splot,  $\text{Ab(Dao)} - \text{Ab(Splot)}$ . As can be seen in this Table, the agreement between the two methods is good for most of the elements, always better than the typical errorbars given for our measurement of the corresponding elements, and usually below 0.10 dex. The differences are higher for those elements with fewer lines (e.g. Na I and Ti I), which increases the weight of the scatter among lines. Let us note in particular that elements such as Ca I or Ti I do not seem to be affected by the method used for equivalent width measurement in a systematic direction, so that the strong underabundances found for these elements (with respect to the galactic trends) are robust against EW systematics.

**Table A.1.** Comparison of the equivalent widths derived from DAOSPEC and Iraf-Splot task for six of our sample stars.

Line	Element	RGB_522		RGB_546		RGB_664		RGB_666		RGB_720		RGB_1055	
		Dao	Splot	Dao	Splot	Dao	Splot	Dao	Splot	Dao	Splot	Dao	Splot
6300.31	O1	-	-	-	-	96	108	-	-	-	-	-	-
6274.66	V1	173	159	118	85	171	156	-	-	-	-	75	54
6285.17	V1	140	172	92	111	170	159	71	61	-	-	61	-
6199.19	V1	206	205	126	128	193	212	90	186	-	-	79	72
6292.82	V1	167	186	111	116	174	192	70	90	-	-	-	-
6224.51	V1	134	130	77	76	147	135	44	54	-	-	32	24
6251.82	V1	170	184	119	118	165	173	69	24	-	-	-	-
6150.15	V1	167	169	92	91	178	183	44	44	-	-	54	53
6135.37	V1	146	155	74	51	150	138	47	51	-	-	40	-
6119.53	V1	139	153	85	94	136	139	63	96	-	-	65	89
6452.32	V1	103	106	43	44	43	64	21	32	44	42	-	-
6531.41	V1	105	106	41	37	109	109	-	-	45	38	-	-
6357.29	V1	37	40	-	-	-	-	-	-	-	-	-	-
6222.58	Y1	-	-	-	-	38	54	-	-	-	-	-	-
6435.01	Y1	78	88	28	44	77	67	22	47	21	17	-	-
6613.73	Y2	-	-	-	-	-	-	-	-	94	-	-	-
6496.90	BA2	249	267	218	210	239	238	209	206	200	187	-	-
6141.73	BA2	260	281	220	220	272	268	201	207	-	-	-	-
6572.80	CA1	216	229	156	156	231	218	125	145	124	110	107	120
6162.19	CA1	308	334	234	229	312	319	211	215	-	-	198	194
6169.56	CA1	179	175	140	148	188	173	143	167	-	-	134	142
6169.04	CA1	162	147	128	111	163	138	119	137	-	-	106	99
5601.29	CA1	201	204	150	154	206	203	125	129	156	150	117	129
6493.79	CA1	192	195	165	161	196	195	117	107	148	144	130	125
6166.44	CA1	144	140	105	84	143	143	98	99	-	-	104	111
6499.65	CA1	159	161	115	112	153	146	114	116	117	81	101	106
6161.30	CA1	151	172	129	114	165	158	75	55	-	-	81	88
6455.61	CA1	126	126	94	88	119	122	85	74	74	93	76	76
6439.08	CA1	224	227	187	189	241	228	182	163	197	193	163	163
6471.67	CA1	164	176	140	142	168	149	117	116	143	151	122	134
6508.84	CA1	72	72	-	-	54	74	-	-	28	42	-	-
6282.60	CO1	152	180	109	112	177	177	-	-	-	-	55	22
6117.00	CO1	-	-	-	-	-	-	-	-	-	-	29	18
5647.24	CO1	80	85	45	43	77	73	36	39	54	56	31	29
6330.10	CR1	141	152	95	85	148	155	75	44	-	-	69	74
6362.88	CR1	-	-	101	98	168	153	64	29	-	-	66	55
5787.93	CR1	102	107	69	71	110	101	39	-	68	85	47	51
5783.07	CR1	92	94	60	57	90	88	25	-	41	54	32	-
5782.13	CU1	199	172	126	113	202	160	100	98	121	123	-	-
6358.69	FE1	241	186	170	173	214	212	119	-	-	-	164	-
6498.95	FE1	183	192	156	152	200	184	137	134	157	153	126	131
6574.25	FE1	160	162	144	153	171	150	112	108	129	119	107	115
6581.22	FE1	138	114	97	93	150	187	92	110	88	108	75	72
6430.86	FE1	243	244	201	194	257	250	195	203	208	237	164	155
6151.62	FE1	140	149	118	121	136	135	100	13	-	-	92	98
6335.34	FE1	217	211	183	174	220	215	170	158	-	-	148	144
6297.80	FE1	180	191	147	151	193	205	137	160	-	-	123	117
6173.34	FE1	169	189	149	159	170	165	135	146	-	-	124	126
6421.35	FE1	214	221	187	189	222	215	200	197	194	196	157	159
6481.88	FE1	151	157	132	125	163	149	126	128	123	126	108	102
6392.54	FE1	88	86	-	-	90	79	32	26	-	-	-	-

**Table A.1.** Comparison of the equivalent widths derived from DAOSPEC and Iraf-Splot task for six of our sample stars.

Line	Element	RGB_522		RGB_546		RGB_664		RGB_666		RGB_720		RGB_1055	
		Dao	Splot	Dao	Splot	Dao	Splot	Dao	Splot	Dao	Splot	Dao	Splot
6392.54	FE1	88	86	-	-	90	79	32	26	-	-	-	-
6608.04	FE1	99	110	80	67	128	119	32	32	95	83	-	-
6494.99	FE1	261	283	229	232	274	270	222	220	224	241	174	183
6393.61	FE1	224	229	-	-	235	232	188	-	-	-	167	161
6344.16	FE1	201	185	154	160	201	180	115	127	-	-	-	-
6593.87	FE1	181	191	154	164	192	197	141	177	154	181	120	117
5701.56	FE1	174	170	146	139	185	174	140	142	131	125	130	122
6609.12	FE1	155	163	136	148	168	157	87	94	155	133	122	108
6475.63	FE1	134	132	108	113	142	132	97	94	125	79	89	94
6137.70	FE1	261	264	211	197	268	261	200	218	-	-	174	168
6322.69	FE1	153	165	136	135	156	166	135	174	-	-	116	108
6575.04	FE1	167	179	133	147	179	167	137	161	112	73	102	107
6200.32	FE1	160	162	131	120	150	146	121	129	-	-	128	120
6180.21	FE1	141	152	114	117	133	153	94	133	-	-	94	106
6518.37	FE1	132	141	114	121	144	126	112	125	95	109	93	84
6355.04	FE1	-	-	141	128	183	170	130	102	-	-	127	117
6411.66	FE1	161	164	153	146	156	160	137	136	147	180	118	118
6301.51	FE1	152	165	-	-	175	194	150	144	-	-	109	106
6302.50	FE1	128	138	105	112	129	134	87	110	-	-	89	87
6336.83	FE1	159	149	136	134	154	158	138	139	-	-	125	85
6408.03	FE1	-	-	122	114	131	140	118	117	87	105	111	106
5809.22	FE1	105	111	74	83	92	94	60	63	82	86	62	51
6188.02	FE1	84	90	69	71	90	80	57	58	-	-	51	42
6157.73	FE1	126	132	102	94	141	142	93	94	-	-	86	88
6165.36	FE1	79	83	68	57	72	67	77	104	-	-	42	58
6380.75	FE1	87	85	61	73	89	67	66	12	-	-	-	-
6380.75	FE1	87	85	61	73	89	67	66	12	-	-	-	-
5618.63	FE1	107	121	68	60	97	96	61	65	69	80	60	56
5638.27	FE1	121	104	96	89	128	114	96	90	87	92	82	70
5635.82	FE1	81	52	48	42	80	64	45	47	54	22	40	-
5641.45	FE1	115	95	93	84	-	-	77	75	81	63	69	63
5814.81	FE1	65	54	-	-	39	33	-	-	-	-	25	-
5717.83	FE1	112	104	90	85	115	104	77	70	93	76	67	66
5705.47	FE1	72	66	48	42	74	54	33	31	-	-	38	38
5691.50	FE1	90	94	56	60	79	73	36	35	62	60	43	41
5619.61	FE1	-	-	41	37	76	70	44	34	54	47	29	23
5806.73	FE1	86	83	66	82	83	75	50	-	62	82	45	46
5679.02	FE1	83	77	-	-	83	79	59	54	66	89	52	46
6597.56	FE1	53	65	37	35	83	68	40	32	56	75	37	27
6469.19	FE1	128	138	75	213	109	100	62	70	92	200	55	58
5633.95	FE1	87	92	64	63	83	78	57	58	56	51	52	46
6516.08	FE2	61	98	57	59	58	68	-	-	-	-	60	64
6432.68	FE2	33	27	40	37	51	38	47	51	53	56	-	-
6149.25	FE2	-	-	-	-	-	-	31	54	-	-	-	-
6247.56	FE2	46	55	43	41	41	46	57	50	-	-	38	53
6456.39	FE2	51	57	62	58	56	66	71	55	52	70	64	63
6320.43	LA2	100	84	83	72	90	75	40	-	-	-	-	-
6390.48	LA2	67	86	65	85	72	63	43	72	-	-	-	-
6390.48	LA2	67	86	65	85	72	63	43	72	-	-	-	-
5711.09	MG1	148	134	119	116	155	149	116	116	110	119	104	103
5688.22	NA1	190	137	125	82	198	146	100	76	119	89	37	-

**Table A.1.** Comparison of the equivalent widths derived from DAOSPEC and Iraf-Splot task for six of our sample stars.

Line	Element	RGB_522		RGB_546		RGB_664		RGB_666		RGB_720		RGB_1055	
		Dao	Splot	Dao	Splot	Dao	Splot	Dao	Splot	Dao	Splot	Dao	Splot
5682.65	NA1	159	148	82	64	159	159	57	68	68	54	45	45
6160.75	NA1	88	67	-	-	94	79	32	42	-	-	-	-
6154.23	NA1	59	69	-	-	78	67	24	20	-	-	-	-
6327.60	NI1	139	135	102	106	131	135	84	110	-	-	73	71
6128.98	NI1	109	127	78	75	116	122	68	70	-	-	60	56
6314.67	NI1	139	150	122	125	150	133	116	165	-	-	100	91
6482.81	NI1	124	117	94	98	127	127	89	88	112	118	77	77
6532.89	NI1	74	83	53	53	89	84	33	36	49	36	-	-
6586.32	NI1	110	117	99	94	-	-	105	125	88	106	82	96
6175.37	NI1	68	72	40	51	44	27	36	57	-	-	-	-
6305.67	SC1	209	266	86	101	212	219	58	60	-	-	29	28
6604.60	SC2	91	102	82	80	115	88	31	48	125	-	60	53
5640.99	SC2	113	97	82	77	124	110	85	79	85	103	72	68
5669.04	SC2	136	138	114	127	140	144	93	96	85	104	82	87
5667.15	SC2	84	85	58	59	86	79	69	53	60	72	54	51
6245.62	SC2	95	85	66	69	101	112	76	101	-	-	57	64
5665.56	SI1	66	75	28	28	54	57	32	41	35	42	31	16
5690.43	SI1	55	56	31	32	59	54	29	-	49	45	36	39
5793.07	SI1	49	40	38	36	48	51	39	39	-	-	25	30
6599.11	TI1	128	142	82	86	147	138	-	-	-	-	34	44
6126.22	TI1	152	170	114	121	166	170	81	130	-	-	72	92
6261.11	TI1	235	248	151	156	231	234	75	120	-	-	103	104
6554.24	TI1	140	134	83	86	146	123	68	66	84	56	61	64
6303.77	TI1	110	131	59	58	114	109	50	-	-	-	-	-
6258.10	TI1	221	182	139	152	232	233	114	-	-	-	108	110
6556.08	TI1	152	150	100	94	169	151	83	71	90	81	64	58
5648.58	TI1	82	73	34	31	77	68	-	-	36	31	23	18
6559.59	TI2	83	86	61	65	84	52	60	49	88	70	57	48
6491.56	TI2	103	107	75	79	91	87	67	81	83	86	59	63
6606.95	TI2	46	57	-	-	71	83	-	-	-	-	-	-

**Table A.2.** Absolute differences  $Ab(Dao) - Ab(Splot)$  and the average value (see text).

Element	RGB_522	RGB_546	RGB_664	RGB_666	RGB_720	RGB_1055	Average Difference
CA1	-0.03	0.13	-0.04	0.03	-0.06	-0.09	$-0.01 \pm 0.08$
CR1	-0.08	0.03	0.10	-0.05	-0.05	0.11	$0.01 \pm 0.08$
FE1	-0.11	0.01	0.10	-0.01	-0.06	0.00	$-0.02 \pm 0.07$
FE2	-0.13	-0.06	-0.02	0.04	-0.05	-0.10	$-0.05 \pm 0.06$
NA1	0.08	0.09	0.18	-0.06	0.06	-0.06	$0.05 \pm 0.09$
NI1	-0.03	-0.06	0.09	0.04	-0.12	-0.09	$-0.03 \pm 0.08$
SI1	-0.05	0.01	-0.01	0.07	0.20	-0.03	$0.03 \pm 0.09$
TI1	-0.06	0.00	0.14	0.02	-0.16	-0.10	$-0.03 \pm 0.10$
TI2	-0.18	-0.07	0.13	0.0	0.13	0.06	$0.01 \pm 0.12$
V1	-0.05	0.02	0.10	-0.22	-0.10	-0.09	$-0.06 \pm 0.11$

